Model-based Deformable Registration of MRI Breast Images with Enhanced Feature Selection

MODEL-BASED DEFORMABLE REGISTRATION OF MRI BREAST IMAGES WITH ENHANCED FEATURE SELECTION

BY

SHADI EMAMI ABARGHOUEI, B.Sc.

A THESIS

SUBMITTED TO THE DEPARTMENT OF BIOMEDICAL ENGINEERING

AND THE SCHOOL OF GRADUATE STUDIES

OF MCMASTER UNIVERSITY

IN PARTIAL FULFILMENT OF THE REQUIREMENTS

FOR THE DEGREE OF

MASTER OF APPLIED SCIENCE

Master of Applied Science (2014) McMaster University
(Biomedical Engineering) Hamilton, Ontario, Canada

TITLE:	Model-based Deformable Registration of MRI Breast Images with Enhanced Feature Selection
AUTHOR:	Shadi Emami Abarghouei B.Sc., (Electrical Engineering) Isfahan University of Technology, Isfahan, Iran
SUPERVISOR:	Dr. Shahin Sirouspour
NUMBER OF PAGES:	xii, 84

To my beloved

Mother

Abstract

This thesis is concerned with model-based non-rigid registration of single-modality magnetic resonance images of compressed and uncompressed breast tissue in breast cancer diagnostic/interventional imaging. First, a volumetric registration algorithm is developed which solves the registration as a state estimation problem. Using a static deformation model. To reduce computations, the similarity measure is calculated at some specific points called control points. These control points can be from a low resolution image grid or any irregular image grid. Our numerical analysis has shown that control points placed in the area without much information; i.e with small or no changes in image intensity, yield negligible deformation. Therefore, the selection of the control points can significantly impact the accuracy and computation complexity of the registration algorithms. An extension of the speeded up robust features (SURF) to 3D is proposed for enhanced selection of the control points in deformable image registration. The impact of this new control point selection method on the performance of the registration algorithm is analyzed by comparing it to the case where regular grid control points are used. The results show that the number of control points could be reduced by a factor of ten with new selection methodology without sacrificing performance. Second image registration method is proposed in which, based on a segmented pre-operative image, a deformation model of the breast

tissue is developed and discretized in the spatial domain using the method of finite elements. The compression of the preoperative image is modeled by applying smooth forces on the surface of the breast where compression plates are placed. Image registration is accomplished by formulating and solving an optimization problem. The cost function is a similarity measure between the deformed preoperative image and intra-operative image computed at some control point and the decision variables are the tissue interaction forces.

Acknowledgements

First and foremost, I would like to express my deepest appreciation to my supervisor, Dr. Shahin Sirouspour for his support, encouragement, and invaluable comments. The completion of this master thesis would have not been possible without his supervision. The administrative team of the Biomedical Engineering deserves my special thanks for their help in many matters.

Special thanks to Dr. Bahram Marami for his impressive work, his comments and for his constant help. My kind regards to my dear friends, Elham Karami and Foad Sohrabi for their incredible intellectual supports, suggestions and patience. Much thanks my dearest friend Anna Iranidoust for her kindness, and for always cheering me up.

I take this opportunity to thank my dear brothers, Babak and Pouyan for their support in all stages of my life. Last but not the least, my heartfelt appreciation goes to my beloved mother, Shahin, for her endless love and support through my life. I dedicate this thesis to her with all my love.

Abbreviations

CR	Correlation Ratio
CT	Computed Tomography
FFD	Free-Form Deformation
FE	Finite Element
FEM	Finite Element Method
FLE	Fiducial Localization Error
FRE	Fiducial Registration Error
IRTK	Image Registration Toolkit
MI	Mutual Information
MR	Magnetic Resonance
MRI	Magnetic Resonance Imaging
NCC	Normalized Correlation Coeffcient
NMI	Normalized Mutual Information
PET	Positron Emission Tomography
RBF	Radial Basis Functions
SAD	Sum of Absolute Difference
SIFT	Scale Invariant Feature
SNR	Signal to Noise Ratio

SSD	Sum of Squared Difference
SURF	Speeded Up Robust Features
SVD	Singular Value Decomposition
TPS	Thin-Plate Splines
TRE	Target Registration Error
US	Ultrasound
2D	Two-Dimensional
3D	Three-Dimensional

Contents

List of Figures

Chapter 1

Introduction

1.1 Motivation

Breast cancer is the most common type of cancer in women worldwide. The treatment of breast cancer is most effective when it is diagnosed at early stages (Suetens, 2009). With significant advances in the medical imaging technologies in the past couple of decades, it is now possible to acquire incredible amount of information about internal organs, their structure and functionality. X-ray computed tomography, ultrasound (US), magnetic resonance imaging (MRI), positron emission tomography (PET), photon emission computed tomography (SPECT) and functional MRI (fMRI) are the most common imaging modalities today. These imaging techniques capture different properties of the tissue by using different sensors and offer a varying trade-off among the resolution and quality of the obtained image, the ease of use, speed, and cost. PET, SPECT, and fMRI deal with metabolic measurement (Galloway Jr *et al.*, 1992). MRI (mostly for soft tissue observation), CT (mostly for bony structures) and US provide detailed structural information about internal organs (Suetens, 2009). It is because of these differences in imaging capabilities that often a single modality may not provide sufficient information or be effective in clinical diagnostic and/or interventional applications. In such cases, information from multiple sources may have to be used to provide the physician with a more comprehensive picture of the underlying condition.

Among all different imaging modalities, X-ray computed tomography (CT) has been the most common tool for breast screening. However, CT has poor sensitivity in tumor detection in young adults with dense breast, giving rise to a vital need for alternative screening methods (Suetens, 2009). High resolution MR imaging has proven effective for diagnosis and treatment planning of breast cancer (Marami, 2013). The use of high quality of MRI in imaging is limited due to their incompatibility with surgical instruments and long acquisition times. Similarly concerns over harmful exposures in the case of CT imaging, restrict its use. In contrast, US can be used easily in the operating room along with other equipment without having any harmful side effects. However, US has a limited field of view and its image quality is inferior to that of MR and CT. As a result its sensitivity of detection in a small region is low (Solberg *et al.*, 2007). Given the strengths and weaknesses of various imaging technologies, fusion of data from multiple imaging modalities in the so-called image registration process has become popular in medical imaging.

Registration could be useful even with single modality imaging, when images are captured over a period of time. This is due to the fact that the patient position and orientation with respect to the imaging device can change and/or the tissue could deform over time. Image resolution may also be subject to change. For example, in breast image comparison which is the subject of this thesis, single modal registration of MR images are widely used. In MRI-based breast cancer detection contrast agent must be injected in order to compare the uptake curve which will be different in malignant and benign disease (Heywang-Köbrunner *et al.*, 1997). This injection enhances the intensity of the glandular tissue of the breast and increases the resolution. In addition, benign and malignant tissues brighten differently in presence of the contrast agent. Thus comparing the images taken before and after injection provides invaluable information about the breast.

In breast biopsy, the patient is in the supine position whereas diagnostic images are captured at lateral position which makes the breast to go under large deformation. An additional deformation is caused by applying the stabilizing compression plates prior to biopsy. Moreover, image-based interventions require relatively high update rate, which would not be practical because of long acquisition and processing time. In recent years, interventional MRI systems emerged which can be used during biopsy procedures, but only few image slides with low signal to noise ratio (Chandler *et al.*, 2006). As a result only low resolution images can be provided during the operation. On the other hand, knowing the exact position of the targeted tissue, for example a tumor, prior to inserting the biopsy needle is important, which can not be obtained from the low resolution intra-operative images. Moreover, the huge applied deformation, makes it impossible to compare the normal and compressed images, visually. Registration of preoperative and intra-operative MRI images can help address some of the shortcomings of existing technologies for diagnostic and interventional breast imaging (Marami, 2013).

Many ways for combining image information of preoperative and intra-operative images have been proposed. At the very basic level, one must decide between the possible transformation functions that are mainly divided into rigid, affine and nonrigid transformation. Rigid registration only considers translation and rotation, while affine registration has two more components; i.e., scaling and shearing. Nonlinear mappings, which are the proper choice in case of having large deformation, utilize more complicated functions. These families of mapping functions are capable of mapping straight lines to curves, in addition to rigid mapping.

Given that the breast tissue undergoes high compression between pre-operative and intra-operative images, in the presence of compression plates during the biopsy, non-rigid registration methods would be more suitable for the registration problem in this application. Unlike in rigid registration where all pixels undergo the same transformation in non-rigid registration the deformation of each pixel/voxel can be unique. Image registration is an ill-posed problem which means that several (infinite) solutions for a registration problem may exist. Setting some constraints based on landmarks or solid deformation model can decrease the number of degrees of freedom and hence regulate the problem (Marami, 2013).

1.2 Problem Statement and Solution Approach

One of the most common tools for the breast screening at the diagnosis and treatment stages is MRI (Schnall, 2003). The anatomy and physiology of the female breast pose unique challenges for image registration which requires the characteristics of the tissue behavior to be considered in modeling the deformation (Schnall, 2003). Multiple research studies have confirmed improved cancer detection, diagnosis and evaluation of responses to the therapy using MR imaging methods. Injection of contrast agent can increase the MRI sensitivity in breast cancer detection since malignant tumors and healthy tissues are enhanced differently. The appearance, size ,and shape of the potential cancer lesion is highly dependent on the dynamic of the contrast enhancing agent. The best view may appear within two minutes after injection, then the signal intensity and the apparent boundaries may change dramatically (Azar *et al.*, 2001). In the breast biopsy, the needle causes the breast tissue to deform, which may lead to tumor displacement. In order to decrease possible movements of the tissue due to the needle insertion, the breast is compressed between medial and lateral plates (Azar *et al.*, 2001; Samani *et al.*, 2001). This compression alters the tumor appearance, size and even intensity. As a result it may become difficult to visually compare two breast images taken at different sessions under various compression pressure. The accuracy of tumor localization and estimating its deformation under compression are highly important for the success of the biopsy procedure. On the other hand resolution of the image taken during biopsy is always low due to shortened real-time image acquisition times in order to decrease the patient's discomfort. Consequently, the intra-operative images are less informative than their counterpart preoperative images. All of these aspects together make the registration of the pre-operative and intra-operative images an essential tool in diagnostic/interventional MRI imaging. The goal of this thesis is to develop a deformable image registration model for aligning uncompressed and compressed MRI breast images taken for diagnosis and during biopsy respectively. Ideally, the registration model is fully automatic or requires the minimal interaction. The proposed registration method employs a static linear elastic model of the tissue deformation, discretized by FEM. Biomedical elastic models which use anatomical and physiological properties of the tissue are wide interest in medical image analysis (Marami, 2013). Finite element method (FEM) discretization of the continuum mechanics based model using elastic body deformation is the most popular physical model-based analysis and is more accurate than simpler methods like mass-spring modeling (Marami, 2013). Estimating the material properties of the tissue, identifying the geometry of the object, and defining the boundary condition are the challenging tasks in FE modeling. In our model the breast deformable tissue is considered homogeneous and its material properties are set based on data available in the literature. The geometry of the breast model is defined based on segmentation of the anatomical structures present in the pre-operative images. Lastly boundary conditions are specified as the displacements of the chest wall surface of the segmented breast. The general flow of the family of employed methods is presented in Figure 1.1. After defining the deformation model, the next step is to obtain a proper deformation field that can be applied to the nodes of the FEM to deform the pre-operative image and make it as similar as possible to the intra-operative image.

The task of finding the deformation field obtained by maximizing a similarity measure between the intra-operative (called reference) and pre-operative (called template) image. Computational complexity is reduced by utilizing only a subset of image pixels/voxels rather than the entire image data in the deformation calculations; these are denoted at as *control points*.

The contributions of the thesis can be summarized as

- Enhancing control points selection by developing a new feature selection method
- Extension of a feature point selection method called speeded up robust features (SURF) to 3D
- Patient specific finite element-based deformation model using MR image data.

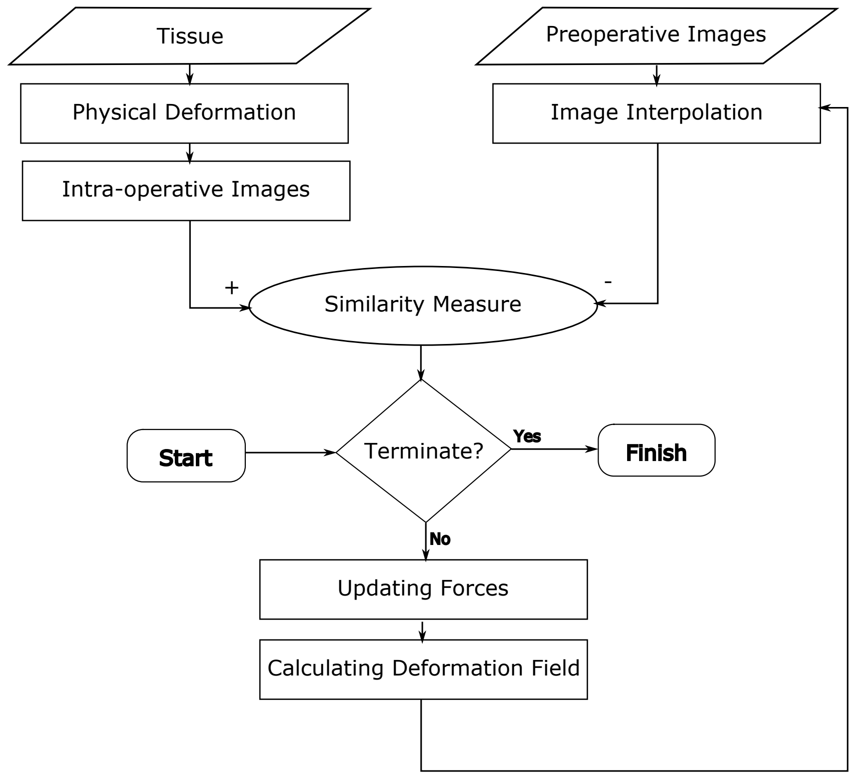

Figure 1.1: General flow of the linear elastic deformation model discretized in the spatial domain using the method of finite element.

- Formulating and solving MRI deformable image registration problem as a non-linear optimization problem

In this thesis, first an enhancement of a previous image registration method (Marami, 2013) is presented. This method estimates the FEM nodal deformation at each iteration using state-estimation techniques for dynamical systems. The parameters are updated based on the calculated error of the similarity measure at selected control points.

Control points, at which the similarity measure between two images are calculated, can be a low resolution regular grid of the image or irregular points. Using regular grids showed that the displacement for the control points in the area without much information is far less than those in the informative areas, i.e areas with image gradient due to rapid change in image intensity. This implies that neglecting areas with small changes in the image intensity may not significantly affect the outcome of the registration. To reduce computations of the optimization, a 3D extension of the so-called SURF (Bay *et al.*, 2006) feature selection method is proposed to select the control points. The SURF algorithm automatically extracts scale and rotation-invariant features with the most information content.Fundamentally, this method relys on the Hessian matrix of the image voxels. Features are voxels with maximum Hessian related values over the predetermined area. Using these new feature points as control points instead of regular grid points, as was done in (Marami, 2013), reduces the number of points needed to achieve the same level of registration quality. Our numerical experiments show that computations are indeed reduced by at least factor of 10 without sacrificing performance.

A new algorithm is proposed for the registration of compressed and uncompressed MRI images of the breast. In this algorithm, first the preoperative image volume (uncompressed breast) is segmented. The segmented image is then used to generate a 3D hexahedron mesh. The boundary condition is set so that the model mimics the actual forces that would be applied to the breast by compression plates. Moreover, the breast tissue position at the chest wall boundary is fixed. The registration algorithm iteratively computes the deformation of the template (preoperative) image T to match it as closely as possible with the reference (intraoperative) image R. At each iteration, the difference between deformed template and the reference image is calculated by obtaining the similarity metric between two images. This error updates the forces that are applied to the surface nodes. The calculated forces are used to deform the finite element mesh. Using the element function, new positions of image grid are calculated , and a new deformed template is obtained via interpolation

1.3 Thesis Organization

The rest of this thesis is organized as follows. Chapter 2 provides a brief review of the existing imaging techniques. The most popular image registration methods are then categorized. Various feature extraction methods proposed in the literature are discussed as well. In Chapter 3, the basics of the FEM is presented and our FEM-based static tissue deformation model is developed. Chapter 4 presents a 3D extension of an existing 2D feature selection method. The selected feature points are used as control points. The impact of having such control points instead of a regular grid point is studied by applying the new control points on an aforementioned method presented in (Marami, 2013). In Chapter 5, our model based image registration model is presented and successfully applied to clinical MRI breast images. Finally, in Chapter 6, the thesis is concluded and some possible directions for further research are discussed.

1.4 Related Publications

• Bahram Marami, Shahin Sirouspour, Suha Ghoul, Shadi Emami Abarghouei, Yue Sun, Aaron Fenster "Non-rigid MRI-TRUS registration in targeted prostate biopsy" in *SPIE Proceedings Vol. 9413: Medical Imaging 2015: Image Processing, 20 March 2015.*

- Shadi Emami Abarghouei, Shahin Sirouspour, " Model-based Deformable Registration of MRI Breast Images by Mimicking the Compression Plate Forces" Abstract submitted for publication in *SPIE Medical imaging 2016 conference.*

Chapter 2

Literature Review

In this chapter a review of medical image registration techniques is presented. First, a brief description of different breast screening modalities is given. Next, the basics of image registration along with its various categories are discussed. Finally, image feature extraction methods are reviewed.

2.1 Medical Imaging

Early detection is vital in treatment of the breast cancer. Breast imaging is valuable for detecting abnormalities. Moreover, in the patients with known malignancies, imaging can be used for choosing the best treatment plan and/or tracking the patient's body response to the therapy (Mann *et al.*, 2008). These days a wide variety of imaging modalities are available for clinical purposes and research studies. X-ray computed tomography (CT), mammography, magnetic resonance imaging (MRI), and ultrasound (US) are the common imaging technologies. The first use of medical images was introduced after the discovery of the X-ray in the late 19^{th} century (Bradley, 2008). This radiation provided valuable information about inner organs of the human body. Ever since, extensive efforts were put into developing new imaging technologies for medical applications. The next few paragraphs focus on the most common modalities in breast imaging.

Mammography which is an imaging technology based on X-ray for acquiring breast images, has proven effective in detecting breast cancer at an early stage (Saslow *et al.*, 2007). Hence, it is widely used for the breast cancer diagnosis (Gøtzsche and Nielsen, 2009). However, an important drawback of mammography, is its low sensitivity in screening breasts in young women, which is composed of dense glandular tissue (Hou *et al.*, 2002; Lee *et al.*, 2010). Aging increases the percentage of fatty tissue, hence making mammography a reliable tool in screening of older women. In young women, there is a high chance of *false positive* and *false negative* detection due to similar appearance of cyst and glandular tissue within mammography screening.

Ultrasound imaging has found a role in complementing mammography for screening of the breast tissue in young patients (Kuhl *et al.*, 2005; Lee *et al.*, 2010). The first clinical use of US in breast imaging was in late twentieth century. In this technique, sound waves above human audible range and their reflection are used for visualization of inner organs (Bradley, 2008). Unfortunately, US suffers from a high *false positive* rate of detection (Lee *et al.*, 2010). Many improvements have occurred in US over the years, which have helped in making it an effective tool in diagnostic and interventional imaging. Doppler ultrasound can be used to acquire colored images by reflecting the sound waves to see how the blood flows through the vessels. The first use of this method for breast screening was proposed in (Adler *et al.*, 1990). During 1970s, MRI was developed. Since then many improvements have occurred in the technology, helping increase the quality, resolution, and speed of MRI imaging. MRI ability in differentiating tissue structures has made it an important tool for screening muscles, the brain and the breast tissue (Bradley, 2008). For acquiring informative MR images with high contrast, contrast agents like gadolinium need to be injected prior to image acquisition (Mann *et al.*, 2008). Contrast-enhanced MRI images of the breast are used for detecting any abnormality in the breast tissue and can help localize the tumor prior to breast cancer surgery (Kuhl *et al.*, 2005). However, the high cost and the low specificity of MRI in detecting some types of cancers have rendered it more of an investigational technique. For example Kuhl *et al.* (2005) has shown that MRI has a low specificity in *Ductal Carcinoma in Situ* which is a common type of the breast cancer.

The use of other imaging techniques such as thermography, PET, and optical imaging is uncommon in clinical applications for breast screening. Among these modalities, thermography has been studied the most, but due to its low sensitivity in detection of the breast cancer, it was never widely used (Lee *et al.*, 2010).

Studies have shown that mammography alone, or mammography combined with breast ultrasound, is ineffective for early diagnosis of the breast cancer. MRI on the other hand has its own limitations in specificity. Image registration can combine information from two or more modalities to to provide a more accurate picture of the imaged tissue. In Figure 2.1, images taken with three modalities, mammography (A), US (B), and MRI (C) are shown.

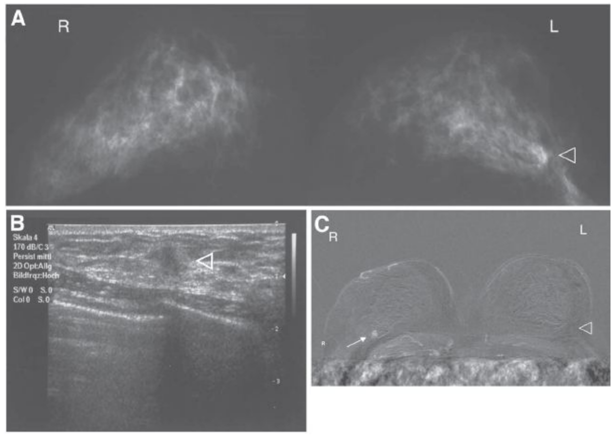

Figure 2.1: Breast imaging modalities - mammogram (A), ultrasound (B), and MRI (c) of a 53-year-old patient history of benign breast biopsy on the left breast. (Kuhl *et al.*, 2005).

2.2 Basics of Image Registration

Image registration is the process of estimating a transformation between two or more images in order to align them. These images can be taken at different times or with various sensors. The image that undergoes the transformation is called "Template"or "Moving"and the other one is the "Reference"or "Target". The template image is transformed in order to increase (decrease) the similarity (difference) between two images (Modersitzki, 2003). In Figure 2.2 an example of a very simple registration is presented. In this figure, the template image 2.2(a) is rotated to align with the reference image 2.2(b). The transformation in this registration a pure rigid rotation. It should be noted that the pixel intensities have not changed after registration.

There are four important considerations in developing an image registration algorithm.

1. Input Image Modality: Based on the reference and template image, the registration methods are categorized as mono-modal or multi-modal. In mono-modal

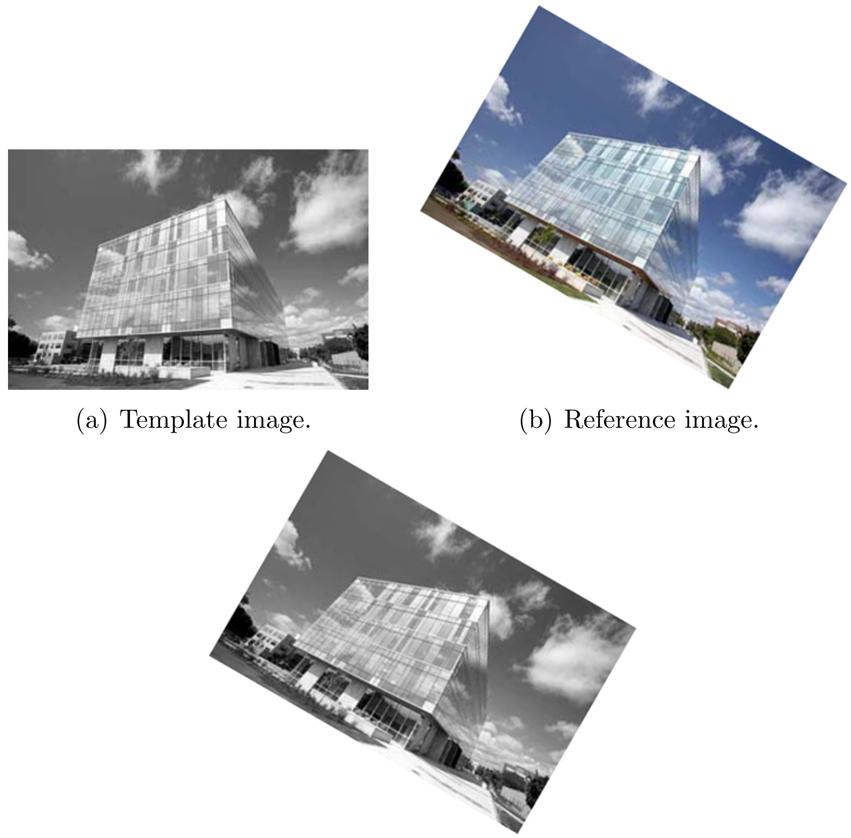

(a) Template image. (b) Reference image.

(c) Template image after registration.

Figure 2.2: A trivial rigid registration example.

registration, both images are obtained using the same imaging technology. These images can be taken at different times or from various view points or in different positions. Multi-modal registration involves images of different modalities. Multi-modal registration is a more complicated task than mono-modal registration, since image content can represent different tissue properties and may not be directly compared. Thus multi-modal registration usually involves an additional step of converting the template and reference images into a common space (Modersitzki, 2003).

In addition to differences in modality, the template and reference images may be of different dimensionality, i.e., 3D to 2D. Such registrations need the transformation function to map the 3D space to 2D.

2. Transformation Function: The choice of the transformation depends on the input image modalities and dimensions, and tissue properties. Rigid registration is used for bony structures like skull whereas non-rigid deformable transformations should generally be used for soft tissues like breast, prostate and liver that can undergo deformation.

3. Similarity Metric: Intensity-based image registration requires a measure of similarity to quantify the distance between the template and reference images. The choice of the similarity metric decides the criteria for this closeness. Various similarity metrics have been used in the literatures (Sarrut and Miguet, 1999). The most popular ones are sum of squared distance (SSD), correlation ratio (CR)(Roche *et al.*, 1998a), correlation coefficient (CC) (Kim *et al.*, 2004), and mutual information (MI) (Maes *et al.*, 1997).

4. Interpolation Methods: Another factor that affects the accuracy of the registration is the choice of interpolation methods for regenerating the deformed image. The most widely used interpolation methods are linear, polynomial (Solomentsev, 2011), and spline interpolation (Bookstein, 1989). More complex interpolations result in more accurate registrations, but the computation time and complexity will increase (Santamaría *et al.*, 2011).

2.3 Image Registration Methods

At a fundamental level, image registration methods can be divided into two main categories: feature-based methods and intensity-based methods (Samavati, 2009).

Feature-based methods find matching points in two images and define a transformation function that maps these points between two images. On the other hand, intensity based methods use pixel intensities information to minimize a cost function of the similarity metrics.

2.3.1 Feature Based Methods

Feature-based methods need a set of corresponding landmarks or features to be selected in the reference and template images (Samavati, 2009; Lester and Arridge, 1999).

The feature point selection itself is divided into extrinsic and intrinsic methods. Artificial fiducials attached to the patient is the basis of extrinsic methods. These objects must be visible and easily detectable by the imaging devices. These artificial markers can be invasive cause patient discomfort.(Maintz and Viergever, 1998). The use of extrinsic feature in 3D images has been limited to the brain and orthopedic (Ellis *et al.*, 1996; Simon *et al.*, 1995). Unlike extrinsic methods, intrinsic ones rely on patient-generated image features (Maintz and Viergever, 1998). Intrinsic methods involve extraction of features from the images (feature extraction stage), as well as descriptor of the selected feature points based on the neighbor pixels (description stage). These features can be selected manually or automatically. An intrinsic feature is a point in the image with a well-defined position which can be detected robustly. Intrinsic features can be surfaces, corners and line endings to isolated points with special characteristics (Samavati, 2009). A defining characteristic of feature detection methods is invariably of the features. A rigid invariant method can find corresponding features between two images that are related through rigid transformation. Using rigid invariant features in the presence of deformation can yield unreliable results.

The most widely used detector is probably the Harris corner detector (Bay *et al.*, 2006). This method uses the eigenvalues of the second moment matrix. However, Harris corners are not scale invariant (Harris and Stephens, 1988). Lowe (1999) introduces scale invariant feature transform (SIFT). SIFT features are scale, rotation and translation invariant.

In SIFT the image is convolved with Gaussian filters at different scales. The difference of Gaussian (DoG) are obtained. The interest points are then taken as maxima/minima of the Difference of Gaussian (DoG) that occur at multiple scales (Lowe, 1999). Although SIFT is widely used, it is a relatively slow method and is very sensitive to change in lighting condition. A number of variants of SIFT have been proposed to increase its performance and speed. These include principal component analysis SIFT (PCA-SIFT)(Ke and Sukthankar, 2004), colored SIFT (CSIFT)(**?**), affine SIFT (ASIFT)(Morel and Yu, 2009) , and speeded up robust features (SURF)(Bay *et al.*, 2006).

PCA-SIFT utilizes the principle component analysis to extract features that are more robust to deformation and has descriptors of smaller dimensions, as it works in the eigenspace (Ke and Sukthankar, 2004). Unlike SIFT which is only applicable to grayscale images, CSIFT can extract features from colored image as well (**?**). ASIFT features are affine invariant so in addition to translation, scaling and rotation, it is also applicable in the presence of sheering (Morel and Yu, 2009). Arguably, SURF is the most popular feature extraction method proposed after SIFT. While its feature matching robustness is slightly less than that of SIFT, SURF is considerably faster. Using integral image concept, SURF greatly increases the speed of feature selection and description phases (Bay *et al.*, 2006).

Most feature selection methods are only applicable when the images are subject to rigid and affine transformations. There are a few methods that can generate descriptors that are invariant under non-rigid transformation, but they are not widely used. Generally in most cases identifiable geometric shapes in medical images are difficult to obtain unless artificial fiducials are attached (Lester and Arridge, 1999), which can be invasive and not desirable for the patient (Maintz and Viergever, 1998).

2.3.2 Intensity-based Methods

Intensity-based registration methods use pixel intensity information to minimize (maximize) a distance (similarity) between the transformed template image and reference image (Kim *et al.*, 2004). Popular similarity/distance measures include SSD, MI, CR, and CC. One of the simplest distance measures is the SSD (Holden *et al.*, 2000; Marami, 2013), which works directly with the difference of the pixel intensities. This makes SSD only applicable to the single-modality problems (Viola and Wells III, 1997). The normalized SSD between the reference (R) and transformed template (T) images is calculated as (Holden *et al.*, 2000)

$$\mathrm{SSD}(\mathbf{u}) = \frac{1}{n}\sum_{i=1}^{n}\left(R_i - T_i\left[\mathbf{u}\right]\right)^2, \tag{2.1}$$

where R and $T[\mathbf{u}]$ are the reference and transformed template image respectively, and n is the number of pixels in the overlap area of the two images. To reduce the sensitivity of this measure to intensity changes due to contrast agent injection, Hill *et al.* (2001) proposes sum of absolute difference (SAD) as

$$\mathrm{SAD}(\mathbf{u}) = \frac{1}{n}\sum_{i=1}^{n} |R_i - T_i\left[\mathbf{u}\right]|. \tag{2.2}$$

CC is another widely used similarity measure in image registration. In CC, pixel intensity values are assumed to be random variables. Kim *et al.* (2004) have shown that the dependency of two images in this scheme is calculated as

$$\mathrm{CC}\left(\mathbf{u}\right) = \frac{\mathrm{Cov}\big(R, T[\mathbf{u}]\big)}{\sqrt{\mathrm{Var}\left(R\right)\mathrm{Var}\left(T\left[\mathbf{u}\right]\right)}} = \frac{\sum_{i=1}^{n}\big(R_i - \bar{R}\big)\big(T_i[\mathbf{u}] - \bar{T}[\mathbf{u}]\big)}{\sqrt{\sum_{i=1}^{n}\big(R_i - \bar{R}\big)^2 \sum_{i=1}^{n}\big(T_i[\mathbf{u}] - \bar{T}[\mathbf{u}]\big)^2}}, \tag{2.3}$$

where *Var* and *Cov* stands for variance and covariance between the reference and template images, respectively. CR, which is a measure of functional dependency between the reference and deformed template (Roche *et al.*, 1998b,a), is another popular method of calculating similarity between two images; it is computed as

$$\mathrm{CR}\left(\mathbf{u}\right) = \frac{\mathrm{Var}\Big(\mathrm{E}\big[T[\mathbf{u}]|R\big]\Big)}{\mathrm{Var}\big(T[\mathbf{u}]\big)}, \tag{2.4}$$

where $E\big[T[u]|R\big]$ measures the part of $T[u]$ that is predicted by R.

Another way of defining dependency of two images is to use the conditional and joint entropy (Studholme *et al.*, 1999)

$$\mathrm{H}\left(T|R\right) = \mathrm{E}_R\left[\mathrm{E}_T\left[log\left(p\left(T|R\right)\right)\right]\right] \tag{2.5}$$

$$\mathrm{H}\left(T,R\right)=\mathrm{E}_{R}\left[\mathrm{E}_{T}\left[log\left(p\left(T,R\right)\right)\right]\right], \tag{2.6}$$

where conditional entropy in(2.5) is a measure of the randomness of T given information about R. Joint entropy can be expressed in terms of marginal and conditional entropy as follows

$$\mathrm{H}(T,R)=\mathrm{H}(T|R)+\mathrm{H}(R). \tag{2.7}$$

Increasing dependency of T on R, decreases $H(T|R)$. However, a small value of $H(T|R)$ may not necessarily imply dependency of T and R, since it could be due to a small H(T) (Studholme *et al.*, 1999). MI between two images measures reduction in the entropy of T and R (Maes *et al.*, 1997)

$$\mathrm{MI}\left(T,R\right)=\mathrm{H}\left(T\right)-\mathrm{H}\left(T|R\right)=\mathrm{H}\left(T\right)+\mathrm{H}\left(R\right)-\mathrm{H}\left(T,R\right)=\mathrm{MI}\left(R,T\right). \tag{2.8}$$

Basically minimizing the joint entropy results in maximizing the MI between images (Pluim, 2000). MI based on the joint marginal probability distribution of images is defined as (Maes *et al.*, 1997)

$$MI\left(R,T\right)=\sum_{r,t}p\left(r,t\right)log\frac{p\left(r,t\right)}{p\left(r\right)p\left(t\right)}. \tag{2.9}$$

While, MI has been successfully used as a similarity measure in multi-modal and mono-modal medical image registration (Al-Azzawi *et al.*, 2010; Gao *et al.*, 2008),it is known to be more effective in multi-modal scenarios (Al-Azzawi *et al.*, 2010; Gao *et al.*, 2008). It should be noted that MI is known to produce unreliable results in small-sized images (Andronache *et al.*, 2008).

2.3.3 Transformation

The geometric relationship between pixels in two images is modeled by "transformation function". The simplest transformation is the rigid registration in which there is no distortion in the image; i.e only rotation and translation are involved. The expression to map the first image coordinates; i.e, x_1,y_1, to the second image coordinates;i.e, x_2,y_2 can be formulated as

$$\begin{bmatrix} x_2 \\ y_2 \end{bmatrix} = \mathbf{R}(\theta) \begin{bmatrix} x_1 \\ y1 \end{bmatrix} + \begin{bmatrix} t_x \\ t_y \end{bmatrix}, \tag{2.10}$$

where $\mathbf{R}$ is the rotation matrix and t_x and t_y are the translation parameters. In the 2D case, $\mathbf{R}$ is defined as

$$\mathbf{R}(\theta) = \begin{bmatrix} cos\ \theta & -sin\ \theta \\ sin\ \theta & cos\ \theta \end{bmatrix}, \tag{2.11}$$

where θ is the rotation angle around the third angle perpendicular to the 2D image plan. In a similar fashion, the mapping function for 3D images is

$$\begin{bmatrix} x_2 \\ y_2 \\ z_2 \end{bmatrix} = \mathbf{R}\left(\theta_x,\ \theta_y,\ \theta_z\right) \begin{bmatrix} x_1 \\ y_1 \\ z_1 \end{bmatrix} + \begin{bmatrix} t_x \\ t_y \\ t_z \end{bmatrix}, \tag{2.12}$$

where $\mathbf{R}$ is defined as

$$\mathbf{R}\left(\theta_x,\ \theta_y,\ \theta_z\right) = \begin{bmatrix} cos\ \theta_z & -sin\ \theta_z & 0 \\ sin\ \theta_z & cos\ \theta_z & 0 \\ 0 & 0 & 1 \end{bmatrix} \begin{bmatrix} cos\ \theta_y & 0 & sin\ \theta_y \\ 0 & 1 & 0 \\ -sin\ \theta_y & 0 & cos\ \theta_y \end{bmatrix} \begin{bmatrix} 1 & 0 & 0 \\ 0 & cos\ \theta_x & -sin\ \theta_x \\ 0 & sin\ \theta_x & cos\ \theta_x \end{bmatrix}. \tag{2.13}$$

In medical applications, rigid registration is mainly used for bony structures (Roche *et al.*, 2000) or soft tissue where deformation is small, e.g., in brain (Schneider *et al.*, 2012). It is also employed as a first step in non-rigid image registrations for aligning two image coordinates (Marami, 2013).

Rigid registration can produce poor accuracy in applications in which tissue undergoes significant deformation; in such cases, non-rigid or deformable registration techniques must be employed. The simplest form of the non-rigid mapping is the affine transformation. In addition to translation and rotation, affine registration can model sheering and scaling as well (Jenkinson and Smith, 2001). For 2D images, affine transformation can be written as

$$\begin{bmatrix} x_2 \\ y_2 \end{bmatrix} = \begin{bmatrix} a_{11} & a_{12} \\ a_{21} & a_{22} \end{bmatrix} \begin{bmatrix} x_1 \\ y_1 \end{bmatrix} + \begin{bmatrix} t_x \\ t_y \end{bmatrix}, \tag{2.14}$$

where matrix of coefficients $a_{11}, a_{12}, a_{21}, a_{22}$ (lets call it matrix $\mathbf{A}$) stands for rotation, sheering and scaling and t_x, t_y (in vector $\mathbf{t}$) model the translation (Pitiot *et al.*, 2006).

In 3D case, the parameters are increased to 12

$$\begin{bmatrix} x_2 \\ y_2 \\ z_2 \end{bmatrix} = \begin{bmatrix} a_{11} & a_{12} & a_{13} \\ a_{21} & a_{22} & a_{23} \\ a_{31} & a_{32} & a_{33} \end{bmatrix} \begin{bmatrix} x_1 \\ y_1 \\ z_1 \end{bmatrix} + \begin{bmatrix} t_x \\ t_y \\ t_z \end{bmatrix}. \tag{2.15}$$

Under affine transformation, straight lines of the image remain straight. Deformable transformations, on the other hand, can map straight lines to curves. The general formula for a deformable function is (Woods *et al.*, 1998)

$$\begin{bmatrix} x_2 \\ y_2 \end{bmatrix} = \begin{bmatrix} f\left(x_1,\ y_1\right) \\ g\left(x_1,\ y_1\right) \end{bmatrix}, \tag{2.16}$$

where f and g are polynomial functions. The basic idea in nonlinear registrations is to find the displacements for a limited number of pixels and approximate deformation of the whole image using interpolation theory(Sotiras *et al.*, 2013). In this thesis, these pixels at which the displacement is calculated are called control points. In addition to polynomial functions, the radial basis functions (RBF) are also widely used for interpolation.

RBFs represent the displacement $u(x)$ at point x as a linear combination of translated radially symmetric functions plus a low-degree polynomial as (Zagorchev and Goshtasby, 2006)

$$\mathbf{u}(\mathbf{x}) = \mathbf{A}\mathbf{x} + \mathbf{t} + \sum_{i=1}^{N} \phi_i(\|\mathbf{x} - \mathbf{p}_i\|), \tag{2.17}$$

where $\mathbf{A}$ and $\mathbf{t}$ are the affine parameters and $\phi(.)$ is called the basis function centered at the known control points. For RBF, these control points can be regular or irregular grid points, and the global deformation is calculated based on the displacement at these points (Zagorchev and Goshtasby, 2006).

The best known RBFs are Gaussian functions and Splines (Bookstein, 1989; Shen and Davatzikos, 2002). The basic function ϕ in the case of Gaussian is defined as (Shen and Davatzikos, 2002)

$$\phi\left(\|\mathbf{x}-\mathbf{p}_i\|\right) = e^{-\frac{\|\mathbf{x}-\mathbf{p}_i\|^2}{\sigma^2}}, \tag{2.18}$$

where σ controls the spatial influence of the Gaussian kernel centered in control points $\mathbf{P}$. Splines are another group of RBFs which are widely used in medical image studies. Thin Plate Splines (TPS) are the most common Splines in which the image is assumed as a thin plate that covers some specfic points called seed points (can be control points or any other selected points). The whole deformation will be obtained by minimizing the bending energy of the plate in order to match the plate to the new positions of the seed points after obtaining corresponding displacements (Maintz and Viergever, 1998; Li *et al.*, 2007). In 2D case, ϕ is represented as (Bookstein, 1989)

$$\phi\left(\|\mathbf{x}-\mathbf{p}_i\|\right) = \|\mathbf{x}-\mathbf{p}_i\|^2 \log\left(\|\mathbf{x}-\mathbf{p}_i\|\right), \tag{2.19}$$

and in 3D as (Bookstein, 1989)

$$\phi\left(\|\mathbf{x}-\mathbf{p}_i\|\right) = \|\mathbf{x}-\mathbf{p}_i\|. \tag{2.20}$$

B-Spline is a popular type of Splines in image registration. In contrast to TPS that can be applied on irregular shapes, B-splines need the seed points to have uniform spacing and are locally controlled (see (Rueckert *et al.*, 1999)). Bsplines are widely used in free form deformation (FFD) method. FFD is combined from a global deformation which is modeled by affine transformation and local deformation based on B-Splines (Rueckert *et al.*, 1999).

2.3.4 Optimization

The registration algorithm can be formulated as a distance minimization (maximization if similarity is used) problem

$$\hat{\mu} = \arg\min_{\mu} C(\mu; I_R, I_T)$$

in which I_R and I_T are the reference and template image respectively. The cost function is the similarity/distance metric and μ contains the decision variables (e.g., the deformation field) (Klein *et al.*, 2007). Registration is an ill-posed problem (Sotiras *et al.*, 2013), means that problem may have an infinite number of solutions. Addition regularization term can help eliminate this problem, but multiple solutions (finite number) may still exist due to local minima if the optimization problem is not convex. The cost in regularized registration can be written as

$$C\left(\mu; I_R, I_T\right) = C_s\left(\mu; I_R, I_T\right) + \omega R\left(\mu\right) \tag{2.21}$$

where C_s is the similarity measure and R is the regularization term. Curvature term, elastic energy and volume preserving penalty have been used in the literature for regularization(Klein *et al.*, 2007).

A widely used method to avoid local minima is multiresolution optimization which is presented in (Maes *et al.*, 1999). In this method low resolution image is used for starting the optimization. Step by step, the resolution is increased as the solution gets closer to the global minimum. To determine the optimal set of parameter $\hat{\mu}$, an iterative optimization strategy is employed (Klein *et al.*, 2007)

$$\mu_{k+1} = \mu_k + a_k d_k, \tag{2.22}$$

where d_k is the search direction at iteration k and a_k is a scaler controlling the step size along the search direction. Many optimization methods can be found in the literature differing in the way that d_k and a_k is computed (see Klein *et al.* (2007)) As an example in gradient descent method the steps are taken in the negative direction of the gradient of the cost function.

$$\mu_{k+1} = \mu_k - a_k g\left(\mu_k\right) \tag{2.23}$$

where $g(\mu_k)$ is the derivative of the cost function evaluated at the current position μ_k.

Chapter 3

A Review of Linear Elastic Deformation Model

In this chapter, first the basic background concepts of finite element model method (FEM) are introduced and then the steps for developing a FEM based linear elastic deformation model is reviewed.

3.1 Background

The complex deformation of the breast as a soft biological tissue is best described by non-linear (Marami, 2013) or linear elastic models (Broit, 1981). Nonlinear models are more accurate but involve many more computations. The first use of elastic deformation models for non-rigid registration was reported in (Broit, 1981).

Conceptually, image registration using a deformation model usually involves application of boundary forces produced from an image similarity measure between the template and reference images to a deformation model until the two images become sufficiently similar. The elastic deformation model ensures smoothness of the resulting deformation (Broit, 1981).

In this thesis a rather simple linear elastic deformation model is used to keep the computations of the algorithm manageable. More complex and accurate nonlinear models may also be employed but any gain in modeling accuracy would most likely be off set by inevitable errors in model parameters and boundary conditions. Tissue to tissue interaction and inhomogeneities due to fat and glandular tissues are also ignored to simplify the model.

3.2 Linear Elastic Deformation Model

Total potential energy of an elastic body, Π, is sum of its strain energy and the potential energy of the external forces. When the elastic model is at its equilibrium point this energy is minimum (Zienkiewicz and Taylor, 2000). For an elastic continuum body with no initial strains or stress Π is defined as

$$\Pi = \frac{1}{2}\int_{\Omega} \boldsymbol{\sigma}^t \boldsymbol{\epsilon} d\Omega + \int_{\Omega} \mathbf{u}^t \mathbf{f} d\Omega. \tag{3.1}$$

The first term is sum of the strain energy where $\boldsymbol{\epsilon}$ is the strain vector and $\boldsymbol{\sigma}$ is the stress vector of the elastic body. The second term represents the potential energy of the external loads. $\mathbf{f}(x, y, z)$ is the force vector, $\mathbf{u}$ is the deformation field and Ω is the volume of the deformable body.

For linear elastic material that undergoes small deformations strain vector, $\boldsymbol{\epsilon}$, is defined as

$$\boldsymbol{\epsilon} = (\frac{\partial u}{\partial x}, \frac{\partial v}{\partial y}, \frac{\partial w}{\partial z}, \frac{\partial u}{\partial x} + \frac{\partial v}{\partial y}, \frac{\partial v}{\partial y} + \frac{\partial w}{\partial z}, \frac{\partial u}{\partial x} + \frac{\partial w}{\partial z}) = \begin{pmatrix} \frac{\partial u}{\partial x} & 0 & 0 \\ 0 & \frac{\partial}{\partial y} & 0 \\ 0 & 0 & \frac{\partial}{\partial z} \\ \frac{\partial}{\partial y} & \frac{\partial}{\partial x} & 0 \\ 0 & \frac{\partial}{\partial z} & \frac{\partial}{\partial y} \\ \frac{\partial}{\partial z} & 0 & \frac{\partial}{\partial x} \end{pmatrix} (u, v, w) = \mathbf{LU}. \tag{3.2}$$

Based on the material property, the stress vector is denoted by $\boldsymbol{\sigma}$ is related to the $\boldsymbol{\epsilon}$. For linearly-elastic materials, this relation is defined as

$$\boldsymbol{\sigma} = \mathbf{D}(\boldsymbol{\epsilon} - \boldsymbol{\epsilon}_0) + \boldsymbol{\sigma}_0, \tag{3.3}$$

where $\boldsymbol{\sigma}_0$ and $\boldsymbol{\epsilon}_0$ are initial stress and strain respectively. However, in our case these initial values are set to be zero. For isotropic material, elasticity matrix of moduli, $\mathbf{D}$, is defined as (Zienkiewicz and Taylor, 2000)

$$\mathbf{D} = \frac{E}{(1+v)(1-2v)} \begin{pmatrix} 1-v & v & v & 0 & 0 & 0 \\ v & 1-v & v & 0 & 0 & 0 \\ v & v & 1-v & 0 & 0 & 0 \\ 0 & 0 & 0 & \frac{1-2v}{2} & 0 & 0 \\ 0 & 0 & 0 & 0 & \frac{1-2v}{2} & 0 \\ 0 & 0 & 0 & 0 & 0 & \frac{1-2v}{2} \end{pmatrix}. \tag{3.4}$$

In this equation scalar E is the Young's modulus representing the elasticity of the material and measures the force (per unit area) that is needed to stretch (or compress) a material sample. Poisson's ratio, v, is the ratio of the perpendicular portion of the strain, of the load, to the strain in the direction of the load and is constrained to be in the range of $-1 < v < \frac{1}{2}$. For absolutely incompressible material $v = \frac{1}{2}$ (Zienkiewicz *et al.*, 1977).

3.3 Finite Element Model

Discretization of continuous problems and subdividing problems to well-defined components is a common method of solving problems when dealing with complex systems. The finite element method is an approximation of continuum problems in which the continuum (elastic body) is divided into a finite number of elements. These elements are inter-connected at nodal points, and the complete solution is obtained through assembling the deformation associated to all of these connected elements (Zienkiewicz and Taylor, 2000). The number of elements along with their size and type of the elements effect the accuracy of the model. In Figure 3.1, 4 most common type of the elements are shown.

In Figure 3.1, a and c possess linear interpolation functions, while b and d are defined with quadratic ones (Felippa, 2008). The accuracy of mesh deformation depends on the number of elements, number of nodes in each element as well as the type of the element. Using elements with more nodal points, e.g., c or d in Figure 3.1, in general will increase the accuracy but at the same time the complexity is increased as well. Moreover, elements with nonlinear interpolation function, e.g. b and d in Figure 3.1, usually improve modeling accuracy at the expense of computational complexity (Felippa, 2008). Therefore, there is a trade off between modeling accuracy and computational cost in choosing the element type (Mafi, 2008).

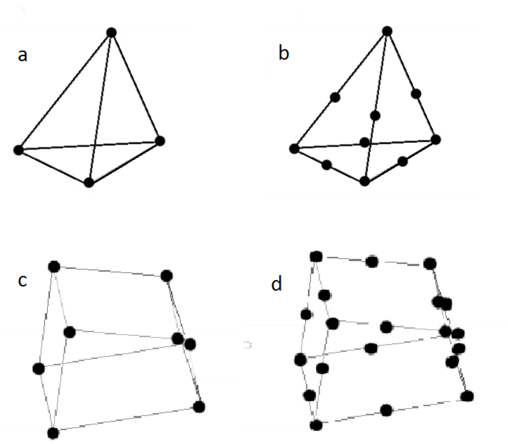

Figure 3.1: Common types of elements, a. linear tetrahedral, b. quadratic tetrahedral, c. trilinear hexahedron, and d. tri-quadratic hexahedron

When applying FEM on the volume of an image each of the image grid points falls inside one element of the FEM mesh. Displacement at any point inside an element is defined as $\mathbf{u}^{el}$, and is a function of displacements of the nodal points of the corresponding element.

$$\mathbf{u}^{el} = \sum_{j=1}^{n} \lambda_j^{el}\,(x, y, z)\, u_j^{el}, \tag{3.5}$$

where λ is the element shape function which defines the deformation pattern inside the elements, and $u^e l_j$ is the nodal points displacement, and n is the number of nodes in an element. Element function is related to the type of the elements that are used for constructing the FEM mesh. The elemental shape function of two types of elements used in this thesis are discussed here.

The shape function for linear tetrahedral elements is given by

$$\lambda_j^{el}(x, y, z) = \frac{1}{6v^{el}}(a_j^{el}x + b_j^{el}y + c_j^{el}z + d_j^{el}), \tag{3.6}$$

where v^{el} is the volume of the tetrahedron. a_j^{el}, b_j^{el},c_j^{el},d_j^{el}, are four coefficients that can be obtained based on the position of the four vertices of the tetrahedron u^{el} (See(Zienkiewicz *et al.*, 1977) for expressions).

For a tri-linear hexahedron element the shape function of the i^{th} node is calculated as (Felippa, 2013)

$$\lambda^{el} = \Sigma_{i=1}^{8} N_i v_i^{el}, \tag{3.7}$$

where

$$N_i^{(e)} = \frac{1}{8}(1 + \varepsilon\varepsilon_i)(1 + \eta\eta_i)(1 + \mu\mu_i), \tag{3.8}$$

Each tri-linear hexahedron element has 8 nodes and ε_i,η_i and μ_i in Equation(3.8) for each node are

ith node	ε_i	η_i	μ_i
1	-1	-1	-1
2	1	-1	-1
3	1	1	-1
4	-1	1	-1
5	-1	-1	1
6	1	-1	1
7	1	1	1
8	-1	1	1

Based on Equations (3.1)–(3.5) total potential energy for the volume of an individual element is written as

$$\prod\left(\mathbf{u}_1^{el},...,\mathbf{u}_n^{el}\right)=\frac{1}{2}\int_\Omega\left(\sum_{i=1}^{n}\sum_{i=1}^{n}\mathbf{u}_i^{el^t}\mathbf{B}_i^{el^t}\mathbf{D}\mathbf{B}_j^{el}\mathbf{u}_j^{el}\right)d\Omega+\int_\Omega\left(\sum_{i=1}^{n}\mathbf{u}_i^{el^t}\lambda_i^{el^t}\mathbf{f}\right)d\Omega, \quad (3.9)$$

where, n is the number of nodes which for tetrahedron elements is 4 and for hexahedrons equals to 8. u_j^{el} and u_j^{el} are the nodal points displacement, D is the elasticity matrix, and B_j^{el} is defined as

$$\mathbf{B}_i^{el}=\boldsymbol{L}_i\lambda_i^{el}. \quad (3.10)$$

At equilibrium point the potential energy is at minimum, thus Π must have a local extermum at u^{el} which means

$$\frac{\partial\prod\left(\mathbf{u}_1^{el},...,\mathbf{u}_n^{el}\right)}{\partial\mathbf{u}_i^{el}}=0 \qquad \text{for} \quad i=1,...,n. \quad (3.11)$$

By substantiating the definition of Π from Equation (3.9) in Equation (3.11), one can write

$$\int_\Omega\sum_{j=1}^{n}\mathbf{B}_i^{el+}\mathbf{D}\mathbf{B}_j^{el+}\mathbf{u}_j^{el}d\Omega+\int_\Omega\lambda_i^{el+}\mathbf{f}d\Omega=0 \quad \text{for} \quad i=1,...,n, \quad (3.12)$$

where L_i is the matrix L at node i and $\Pi(u_1^{el},...,u_n^{el})$ basically determines the contribution of el^{th} element to the energy function of the whole body. By defining $\mathbf{K}_{i,j}^{el}$

as

$$\mathbf{K}_{i,j}^{el} = \int_{\Omega} \mathbf{B}_i^{el^t} \mathbf{D} \mathbf{B}_j^{el} d\Omega, \tag{3.13}$$

and f_i^{el} as

$$\mathbf{f}_i^{el} = \int_{\Omega} \lambda_i^{el^t} \mathbf{f} \; d\Omega. \tag{3.14}$$

Equation (3.12) can be rewritten as a set of linear equations for each element as

$$\mathbf{K}^{el} \mathbf{u}^{el} = -\mathbf{f}^{el}. \tag{3.15}$$

$\mathbf{K}_{i,j}^{el}$ is a 3×3 matrix and would be calculated for each element. In case of modeling with tetrahedron elements K^{el} is a 12×12 matrix and $f^e l$ is a 12×1 vector. Using hexahedron elements with 8 nodes on the other hand results in 24×24 and $24 \times 1, K^{el}$ matrix and f^{el} vector respectively. These matrices are then assembled in a global system

$$\mathbf{K}\mathbf{u} = -\mathbf{f}, \tag{3.16}$$

where $\mathbf{K}$ is the global stiffness matrix, associated with the volumetric mesh and is numerically integrated over the volume of the elastic body (see(Felippa, 2013)). The solutions to this linear system of equation provides the displacement field corresponding to the global minimum of the potential energy. This approach minimizes the energy function and brings it to the equilibrium point as a static problem. However, if one is interested in transient motion and deformational behavior of the object, the dynamic model in which, the velocity dependent damping forces are added to the Equation (3.16), must be used.

Since most anatomical structures in human body are highly deformable, dynamic models are valuable in medical image analysis. In this model the inertial body forces and energy dissipation through velocity dependent damping forces can be added to the static equilibrium Equation (3.16) as

$$\mathbf{M}\ddot{\mathbf{u}} + \mathbf{C}\dot{\mathbf{u}} + \mathbf{K}\mathbf{u} = -\mathbf{f}. \tag{3.17}$$

Here $\mathbf{M}$ is the mass matrix of the elements concentrated at nodes, and $C = \alpha\mathbf{M} + \beta\mathbf{K}$ is the damping matrix for constant value of α and β (Marami, 2013). Having inertia and damping forces added, helps find the solution to the static equilibrium in a numerically effective way. Each element mass of a FE is $M^{el} = \rho V^{el}$, where ρ is the mass density of the object and V^{el} is the element volume.

In order to reduce computations very fast modes of this dynamical system can be discarded without affecting the response at a particular time scale relevant to the application of interest. To this aim, a new variable $\mathbf{u} = \phi\mathbf{x}$ is defined, where columns of ϕ are eigen vectors of $\mathbf{M}^{-1}\mathbf{K}$. Equation (3.17) can be rewritten as

$$\tilde{\mathbf{M}}\ddot{\mathbf{x}} + \tilde{\mathbf{C}}\dot{\mathbf{x}} + \tilde{\mathbf{K}}\mathbf{x} = -\tilde{\mathbf{f}}, \tag{3.18}$$

where $\tilde{\mathbf{M}} = \phi^t\mathbf{M}\phi$, $\tilde{\mathbf{C}} = \phi^t\mathbf{C}\phi$, $\tilde{\mathbf{K}} = \phi^t\mathbf{K}\phi$ are diagonal matrices, and $\tilde{\mathbf{f}} = \phi^t\mathbf{f}$. Now, the dynamic finite element equations are decoupled in (3.18) and each equation describes a vibrational mode of the deformable body (Marami, 2013).

Chapter 4

3D Extension of Speeded Up Robust Features For Enhanced Image Registration

In this chapter a review of a previously proposed image registration method is presented. Next the 3D extension of the speeded up robust features (SURF) is developed to extract image feature points. The extracted features are used as control points in the registration method in order to decrease the computational cost.

Generally, image registration methods find transformation among corresponding images by comparing them through a similarity measure. For example, similarly can be measured by comparing intensities at selected image pixels/voxels, also known as control points. Usually control points are selected from a uniformly distributed coarse grid. While this would provide a convenient choice of control points, it can place some of them in areas with insufficient information content, rendering the registration algorithm less effective. Based on the results presented in (Marami, 2013), areas of image with few discernible features contribute very little to the computed deformation in image registration. In contrast, areas in the image with significant change in intensity and texture due to variations in tissue properties can be very informative for calculation of the deformation in the registration. Logically, rather than distributing the control points uniformly, one should attempt to position them in areas of image with high information content to improve the accuracy of the registration without increasing its computations. In this chapter, an extension of SURF (Bay *et al.*, 2006) to 3D images is presented, which will be utilized for control point selection.

First a brief review of the image registration based on state estimation, introduced in Marami (2013) is presented. Next the 3D extension of SURF is developed. The results of importing the new feature extraction in the deformable image registration algorithm are given at the end of the chapter.

4.1 Image Registration Based on State Estimation

In Marami (2013), registration of two images is posed as a dynamic state estimation problem. In this context, the states are chosen as displacements and velocities of the nodes of a FE mesh which models the deformable tissue. Discrete-time state-space dynamics can be written in the following general form:

$$\mathbf{x}_k = a(\mathbf{x}_{k-1}, \tilde{\mathbf{f}}_{k-1}) + \mathbf{w}_{k-1} \tag{4.1}$$

$$\mathbf{z}_k = h(\mathbf{x}_k) + \mathbf{v}_k \tag{4.2}$$

where $\mathbf{x}_k$ is the vector of deformation states to be estimated at the k^{th} iteration, $\tilde{\mathbf{f}}$ is the input vector(e.g.,external applied forces in tissue deformation models), and

$\mathbf{z}$ is the observation measurement vector. In the proposed registration model, the observations can be the raw gray scale pixel values of the images. Moreover, $a(.)$ and $h(.)$ are two mapping vectors; $a(.)$ in the first equation establishes a relation between the states of deformation at different iterations and $h(.)$ defines the mapping function between the states of deformation and the measurements vector. Moreover, $\mathbf{w}$ and $\mathbf{v}$ are modeling process and measurement noises, respectively.

The general form of a dynamic linear elastic deformation model which contains only m slower modes is given in Equation (3.18). This reduced model, which is used in estimating the deformation states, lowers the computations involved in the algorithm by disregarding the fast vibrational modes of the model. Equation (4.3) represents the time sample, T_s, that must be selected for transforming the continuous-time dynamics in equation (3.18) into discrete-time equations.

$$T_s \simeq \frac{1}{30\sqrt{2}} \frac{2\pi}{\omega_m}. \tag{4.3}$$

Here ω_m is the natural frequency of fastest vibrational mode in the reduced dynamic model of size m. In other words, sampling frequency is chosen to be 30 times the bandwidth of the system defined by the fastest vibrational mode. Using the central difference method in (Bathe, 2006), the discrete-time reduced dynamics can be represented in state-space form as

$$\mathbf{x}_k = \mathbf{A}\mathbf{x}_{k-1} + \mathbf{G}\tilde{f}_{k-1} + \mathbf{w}_{k-1}, \tag{4.4}$$

where, $\mathbf{A}$ and $\mathbf{G}$ are the linear models for the mapping function $a(.)$ presented in equation (4.1), and are defined as

$$A = \begin{pmatrix} 0 & I \\ -\mathbf{W}_1^{-1}\mathbf{W}_3 & -\mathbf{W}_1^{-1}\mathbf{W}_2 \end{pmatrix}; G = \begin{pmatrix} 0 \\ -\mathbf{W}_1^{-1} \end{pmatrix}, \tag{4.5}$$

and

$$\mathbf{W}_1 = \frac{\tilde{\mathbf{M}}_1}{\mathbf{T}_s^2} + \frac{\tilde{\mathbf{C}}_1}{2\mathbf{T}_s} \quad , \mathbf{W}_1 = \tilde{\mathbf{K}}_1 - \frac{2\tilde{\mathbf{M}}_1}{\mathbf{T}_s^2} \quad , \mathbf{W}_1 = \frac{\tilde{\mathbf{M}}_1}{\mathbf{T}_s^2} - \frac{\tilde{\mathbf{C}}_1}{2\mathbf{T}_s}. \tag{4.6}$$

$\tilde{\mathbf{M}}_1$, $\tilde{\mathbf{C}}_1$, $\tilde{\mathbf{K}}_1$ are $m \times m$ matrices obtained from the original $\tilde{\mathbf{M}}$, $\tilde{\mathbf{C}}$, $\tilde{\mathbf{K}}$ matrices corresponding to m slowest modes (see Section 3.3). The size of $\mathbf{A}$ and $\mathbf{G}$ are $2m \times 2m$ and $2m \times m$ respectively.

The registration algorithm in (Marami, 2013) iteratively estimates the deformation of the tissue and computes the deformation of the template image to match it as closely as possible to the reference image. The flowchart of this method is presented in Figure 5.1. The algorithm starts with an initial estimation of the deformation states. At each iteration the estimator compares the reference image and deformed template for providing the estimation of the deformation. A dynamic elastic deformation model introduced in Chapter 3 is utilized to obtain a deformation field in image registration (Marami, 2013).

At the model prediction step (time update) of each iteration the states vector, $\mathbf{x}_{k-1}$, is updated to $\mathbf{x}_k^-$ as

$$\mathbf{x}_k^- = \mathbf{A}\mathbf{x}_{k-1} + \mathbf{G}\tilde{f}_{k-1}, \tag{4.7}$$

The observation model relates the estimated state at each iteration ($\mathbf{x}_k^-$) to the sensor measurements ($\mathbf{z}_k$). In our case the updated states in (4.7), which are the mesh

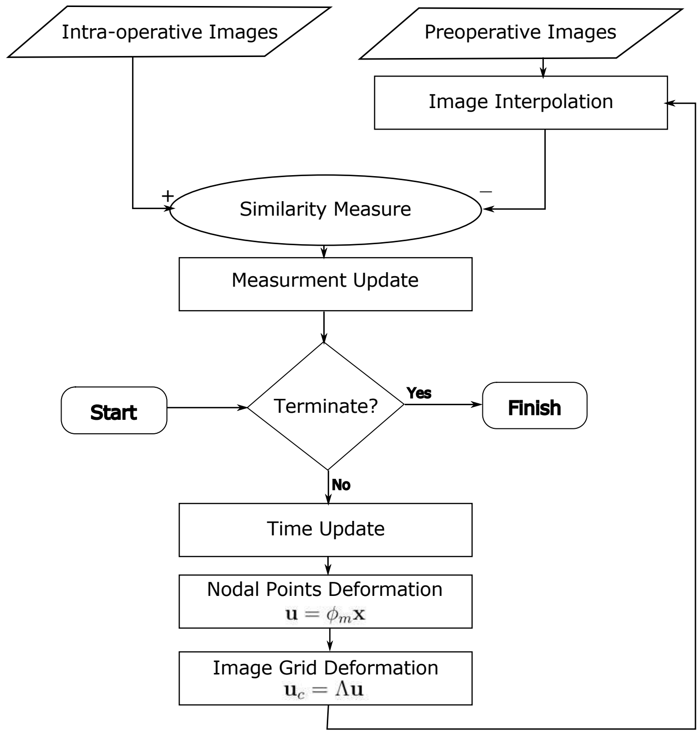

Figure 4.1: Flowchart of the image registration based on state estimation method

nodal point positions and velocities, are used to form the predicted deformed template image. The new image is compared with the reference image and the intensity calculation and error estimation are carried over control points. As previously mentioned, the control points are selected image voxels that are utilized for the image comparison during the registration process. The use of control points instead of considering all of the image voxels significantly reduces the algorithm computation cost. In order to find the new positions of control points the relation between control points and the defined states must be determined. Each control point falls in one specific element. Hence, the deformation of the control points $\mathbf{u}_c$, can be computed from the nodal displacements $\mathbf{u}$, and the elements shape function Λ as

$$\mathbf{u}_c = \Lambda \mathbf{u}. \tag{4.8}$$

The nodal displacements $\mathbf{u}$ are obtained from the states of the reduced dynamic model using $\mathbf{u}_k^- = \phi_m \mathbf{x}_k^-$, in which ϕ_m consists of m columns of ϕ that correspond to m slowest modes of the original model. These steps can be rewritten as one equation which constitutes the observation model

$$\mathbf{z}_k = \mathbf{u}_c = \mathbf{H}\mathbf{x}_k + \mathbf{v}_k, \tag{4.9}$$

$$\mathbf{H} = \Lambda \phi_m. \tag{4.10}$$

Here $\mathbf{v}_k$ is the measurement noise, and The size of $\mathbf{u}_c$, $\mathbf{H}$, and $\mathbf{x}$ are $3n \times 1$, $3n \times 2m$, and $2m \times 1$, respectively.

The observation prediction error, which is the difference between the desired intensity measured at the reference image and intensity of the predicted deformed template image at control points, is computed by finding the gradient of the similarity measure between two images at defined control points

$$d\mathbf{x}_c = -\frac{1}{\gamma}\ \nabla \mathbf{I} x_c(\mathbf{R}, \mathbf{T}(\mathbf{u}_k^-)), \tag{4.11}$$

where $\nabla \mathbf{I} x_c(\mathbf{R}, \mathbf{T}(\mathbf{u}_k^-))$ represents the gradient of the similarity measure. The gradient of the similarity measure can be written as

$$\nabla \mathbf{I} x_c(\mathbf{R}, \mathbf{T}(\mathbf{u})) = g(\mathbf{T}(\mathbf{u}), \mathbf{R}) \nabla \mathbf{T}(\mathbf{u}). \tag{4.12}$$

The $g(.)$ function in (4.12) is the intensity comparison function and $\nabla \mathbf{T}(.)$ is the gradient of the template at defined control points. The intensity comparison functions along with corresponding similarity measures are presented in Table 4.1 (Marami, 2013).

The observation prediction error is used to update the state estimate vector based on the Kalman filtering method by following equation

$$\mathbf{x}_k = \mathbf{x}_k^- + \Gamma d\mathbf{x}_c, \tag{4.13}$$

where Γ is the steady-state Kalman gain, and can be computed off-line, since in this case the control points are fixed at their position and are not updated. To compute the Kalman gain, Q and S, which are the process and measurement error covariances respectively, are defined as

$$\mathbf{Q} = q\mathbf{I}_{2m\times 2m} \qquad \mathbf{S} = s\mathbf{I}_{3n\times 3n} \tag{4.14}$$

where $\mathbf{I}$ is an identity matrix, m is the number of vibrational modes used in the reduced model, and n is the number of control points; q and s are the power of the process and measurement noises respectively and and their ratio determines the resulting Kalman gain. The choice of this ratio depends on the user's relative confidence in the deformation model versus the observation obtained from the similarity/distance measure between images.

The above steps are repeated iteratively until the relative change in the similarity measure between the reference image and the deformed template is less than a specific

	Similarity Measure	g(T(u),R)
SSD	$\frac{1}{2}\int_{\Omega}(T(u)-R)^2 d\Omega$	$i_2 - i_1$
MI	$\int_{R^2} P_u^{T,R}(i_2,i_1) log \frac{P_u^{T,R}(i_2,i_1)}{P_u^T(i_2)P^R(i_1)} di_1 di_2$	$\frac{-1}{\mu(\Omega)} \ [\Psi * (\frac{1}{P_u^{T,R}}\frac{\partial P_u^{T,R}}{\partial i_2} - \frac{1}{P_u^T}\frac{\partial P_u^T}{\partial i_2})](i_2, i_1)$
CR	$1 - \frac{var\left[E[X_u^T \vert X^R]\right]}{var[X_u^T]}$	$\frac{2\Psi*(i_2 - E[X_u^T \vert X^R = i_1] + (CR_y^{T,R} - 1)(i_2 - E[X_u^T])}{var[X_u^T]\mu(\Omega)}$

Table 4.1: Similarity measures and intensity comparison function (Marami, 2013).

value or the total number of iteration exceeds a predefined maximum number.

4.2 3D Extension of Speeded Up Robust Features

In feature based image registration, a feature selection method identifies corresponding features in the template and reference images(Lester and Arridge, 1999). Feature selection methods usually involve two steps. The first step, known as feature selection stage finds the features. The second step, description stage, computes a description for the selected points. Descriptors basically provide information on the neighbor points of the features which is essential for finding matching points between two images. Based on the method of interest, the selected features and their descriptors vary. As an example, features can be the corners, borders or surface of a volume, and descriptors can carry image intensity, gradient or other neighbor pixel informations. Descriptors have to be informative and, at the same time, be robust to noise and deformations. Since descriptors rely on neighbor points arrangement, they are highly sensitive to the type of applied deformation. In contrast, very few methods are available that can work in the presence of deformation in the image. Low accuracy and large computations have prevented widespread use of such methods.

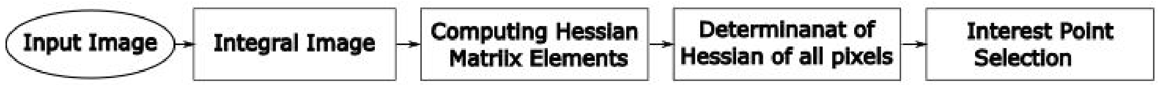

Figure 4.2: Block diagram of the interest point selection

4.2.1 Background

The most important property of an interest point selection method is its repeatability, which means finding the same interest points at different scales and view points (Bay *et al.*, 2006). The most widely used detector is the Harris corner detector (Bay *et al.*, 2006) which uses the eigenvalues of the second derivative of the image. However the extracted feature points in this method are not scale invariant. Many scale invariant methods have been proposed recently. Among them, the Scale Invariant Feature Transform (SIFT)(Lowe, 2004) is a relatively fast method, which has been widely used in many applications. Generally, the high dimensionality of the descriptor is a drawback of SIFT. The Speeded Up Robust Features (SURF) (Bay *et al.*, 2006) has fewer computations than SIFT and has been successfully applied to many feature selection problems. This approach employs a very basic Hessian matrix approximation on the integral images for interest point selection. It achieves a balance between accuracy and computation speed by simplifying the SIFT to its core essentials . In this thesis, an extension of SURF to three dimensional images is proposed and used for control point selection in deformable image registration. A diagram showing steps for interest point selection is presented in Figure 4.2

The interest points in SURF are selected by applying an approximation of the Hessian Filter on the image. Since the Hessian matrix approximation method requires multiple calculations over several areas with different sizes on the image, the use of integral image would reduce the computation dramatically (Bay *et al.*, 2006).

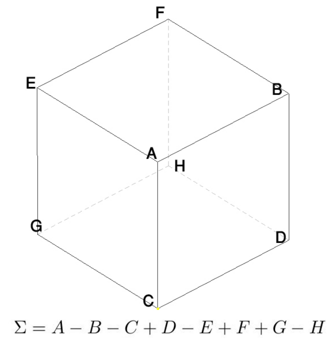

Figure 4.3: Using integral images, it takes only seven additions to calculate the sum of intensities inside a box region of any size.

4.2.2 Integral Image

Each entry of an integral image at each location $\mathbf{X} = (x, y, z)$ represents the sum of all pixel values inside the box formed between the selected point and the origin, that is,

$$I_{\Sigma}(\mathbf{X}) = \sum_{i=0}^{x} \sum_{j=0}^{y} \sum_{k=0}^{z} I(i, j, k). \tag{4.15}$$

After calculating the integral image, only a simple mathematical calculation is needed to obtain the sum of intensities inside any cubic box over the image. This calculation is independent of the size of the box (see Figure 4.3). Therefore, this approach is potentially effective when using multiple large filters.

4.2.3 3D Interest Point Selection Based on Hessian Matrix

The Hessian matrix is a square matrix of second-order partial derivatives of a function, which describes the local curvature of that function. For each point $\mathbf{x} = (x, y, z)$ in $3D$ space which is mapped to the $1D$ space by means of the function f the Hessian matrix is:

$$H(\mathbf{x}) = \begin{pmatrix} \frac{\partial^2 f}{\partial x^2} & \frac{\partial^2 f}{\partial x \partial y} & \frac{\partial^2 f}{\partial x \partial z} \\ \frac{\partial^2 f}{\partial y \partial x} & \frac{\partial^2 f}{\partial y^2} & \frac{\partial^2 f}{\partial y \partial z} \\ \frac{\partial^2 f}{\partial z \partial x} & \frac{\partial^2 f}{\partial z \partial y} & \frac{\partial^2 f}{\partial z^2} \end{pmatrix}. \tag{4.16}$$

In SURF method, in order to have the scale invariant interest points, the Hessian matrix of the image is formed over the image convolved to a Gaussian with predetermined standard deviation (further explanation over scale concept is given in the upcoming paragraphs). Given a point $\mathbf{x} = (x, y, z)$ in an image I, the Hessian matrix is defined as

$$H(\mathbf{x}, \sigma) = \begin{pmatrix} I_{xx}(\mathbf{x}, \sigma) & I_{xy}(\mathbf{x}, \sigma) & I_{xz}(\mathbf{x}, \sigma) \\ I_{yx}(\mathbf{x}, \sigma) & I_{yy}(\mathbf{x}, \sigma) & I_{yz}(\mathbf{x}, \sigma) \\ I_{zx}(\mathbf{x}, \sigma) & I_{zy}(\mathbf{x}, \sigma) & I_{zz}(\mathbf{x}, \sigma) \end{pmatrix}, \tag{4.17}$$

where I_{xx} denotes the convolution of the Gaussian second order derivative with the image I; i.e., $\frac{\partial^2}{\partial x^2} g(\sigma)$, similarly for the rest of the elements. While Gaussians are the optimal filters in scale-space analysis, in practice they have to be discretized and cropped. Thus, Guassians are non ideal filters. Consequently, Bay *et al.* (2006) introduced an alternate for approximating and quick calculation of the Gaussian second order derivative. In order to have the visual understanding of the model let's take a look at the model in 2D. Hence, for now the image is in 2D space and the Hessian matrix is a 2×2 matrix containing the I_{xx}, I_{xy}, I_{yx}(equals to I_{xy}), and I_{yy} elements (first row in Figure 4.4). D_{xx}, D_{xy}, and D_{yy} are the approximation of these elements which are displayed in second row in Figure 4.4. The new approximated Hessian matrix is

$$H(\mathbf{x}, \sigma) = \begin{pmatrix} D_{xx}(\mathbf{x}, \sigma) & D_{xy}(\mathbf{x}, \sigma) \\ D_{yx}(\mathbf{x}, \sigma) & D_{yy}(\mathbf{x}, \sigma) \end{pmatrix}, \tag{4.18}$$

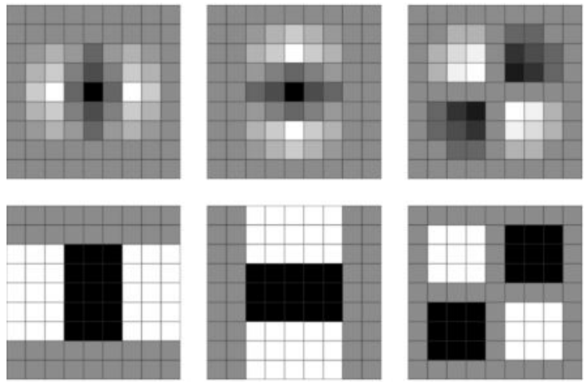

Figure 4.4: left to right: Gaussian second order partial derivatives in x, y and xy directions (first row) and their approximation (second row)

These new elements can be calculated easily. For calculating each of the new estimated parameters only a simple calculation over the white and black area is required. In $3D$ the approximation is done similarly. This time, $3D$ boxes are used to approximate the Gaussian second order derivatives. The new approximated filters are presented in Figure 4.5 and the new Hessian matrix is defined as

$$H(\mathbf{x},\sigma) = \begin{pmatrix} D_{xx}(\mathbf{x},\sigma) & D_{xy}(\mathbf{x},\sigma) & D_{xz}(\mathbf{x},\sigma) \\ D_{yx}(\mathbf{x},\sigma) & D_{yy}(\mathbf{x},\sigma) & D_{yz}(\mathbf{x},\sigma) \\ D_{zx}(\mathbf{x},\sigma) & D_{zy}(\mathbf{x},\sigma) & D_{zz}(\mathbf{x},\sigma) \end{pmatrix}. \tag{4.19}$$

The SURF interest points are those with maximum absolute value of determinant of the Hessian matrix. The SURF method requires the calculation of the determinant of the Hessian of the image. Feature points are selected based on obtaining the determinant of the Hessian matrix for each point; i.e,

$$S = \mid det(H) \mid . \tag{4.20}$$

For calculating the determinant first the Hessian matrix elements must be computed which is done by finding the summation of all the pixels in each white and black areas of boxes in Figure 4.5. D_{xx}, D_{yy}, and D_{zz} are calculated as

$$\sum_{\mathbf{i}\in A} I(\mathbf{i}) - 2\sum_{\mathbf{j}\in B} I(\mathbf{j}), \tag{4.21}$$

where A is the black area and B is the gray area and **i** and **j** are the pixels located in each area. D_{xy}, D_{yz}, and D_{xz} equal to

$$\sum_{\mathbf{i}\in A} I(\mathbf{i}) - \sum_{\mathbf{j}\in B} I(\mathbf{j}) \tag{4.22}$$

. The determinant can now be obtained as

$$\mid det(H) \mid = D_{xx}D_{yy}D_{zz} - DxxD_{yz}^2 - DyyD_{xz}^2 - DzzD_{xy}^2 + 2D_{xy}D_{yz}D_{xz} \tag{4.23}$$

After computing the defined determinant for all image voxels, those with maximum absolute value over their neighbors that can also pass a fixed threshold are selected as feature points of the image.

We also talked about the change of scale in the applied filters. In order to have the interest points selected invariant to the scale, the above mentioned filters are applied on image, in various sizes. Each filter size refers to different standard deviation (σ) of the Gaussian which determines the sharpness/ blurriness of the image, and affects the type of interest points that are selected by each set of filters. Each filter is applied to all of the image voxels, and the Hessian determinant is computed for them. The determinant values are compared and those with maximum value over their neighbors (obtained using the same filter size) which can also pass a fixed threshold are selected as feature points of the image. As the size of the filters increases (larger σ) less points are selected. Here is where use of integral image is useful. Using integral image, instead of repeating Equations (4.21) and (4.22) for each pixel the simple summation presented in Figure 4.3 is required per pixel. Thus with no doubt using integral image as the input of the box filters will highly increase the speed.

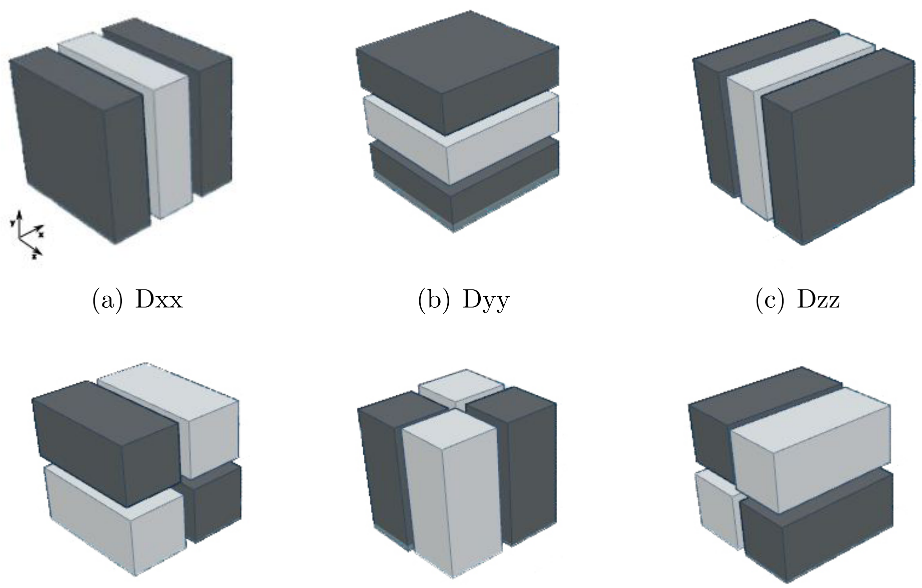

(a) Dxx (b) Dyy (c) Dzz

(d) Dxy (e) Dxz (f) Dyz

Figure 4.5: the approximation of Gaussian second order partial derivatives in x-direction, y-direction and xy-direction using box filters.

.

4.2.4 Control Points Selection

The feature points obtained by applying SURF method on the image are used as control points in the method introduced in Section 4.1. (Marami, 2013) illustrated that the deformation field associated with regions of image with low information content is far less than those at highly informative areas. This motivates selection of a non-uniform grid for control points that concentrate them in areas of high information content in order to improve the quality of registration without increasing its computation cost.In this thesis, the 3D SURF method is used for choosing the control points of the deformable image registration algorithm.

4.3 Experiments and Results

In this section, the effect of having control points selected by feature extraction method versus the regular grid points on the performance of the image registration algorithm is studied. The proposed feature selection method presented in Section 4.2 is employed on the registration algorithm in Section 4.1 and and the results are compared to the case where a uniform grid for the control points is used, as in (Marami, 2013).

3D MR images of compressed and uncompressed breast of a healthy middle-aged women are registered using the proposed method (Figure 4.6). The images have been captured using a GE Discovery MR750 3.0 T MRI scanner. The MRI volumes have been taken in prone position. The image resolution and voxel sizes are $512\times512\times240$ and $0.7031\times0.7031\times1.1$ mm respectively. A sagital view of the template image with the selected control points over 10 slices is shown in Figure 4.7.

The total number of the selected feature points in the volume is 1300. Extracting these interest points took less than $6s$ and can be done prior to the registration. By adjusting the threshold for the Hessian determinant the number of selected points will change. By trial and error it is found out that a threshold value of 0.000002, yields

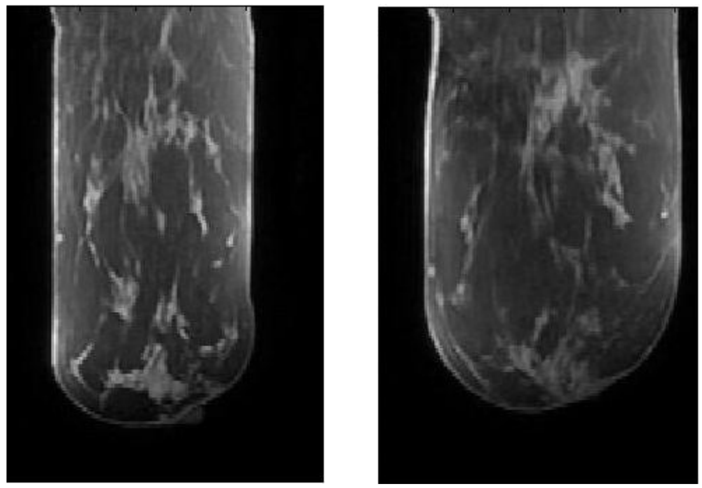

(a) Reference Image (b) Template Image

Figure 4.6: Reference(intra-operative) and Template(pre-operative) Images.

satisfactory results; which means that the points with smaller Hessian determinant than this threshold will be ignored. Increasing the threshold would result in fewer control points which may result in loosing information in some parts of the image. Having more control points on the other hand, may yield too many control points which would increase the computations.

A cubic finite element mesh of tetrahedral elements which encompasses the entire volume of the compressed breast images is created using COMSOL software (Inc, 2013). The mesh has 21151 elements with 4206 nodal points. E and μ are set to 3000 pa and 0.49, respectively. The mass density is set to $\rho = 0.95\ g/cm^3$. The process to measure noise power ratio in the Kalman filter is set to $q/s = 1000$ and the parameter m in model reduction is set as 500. . It should be pointed out that since the mesh is cubic and is built over the whole volume of the image (see Figure4.9) including the background area, having the control points located only on the breast area results in an inaccurate deformation since there is no information available about

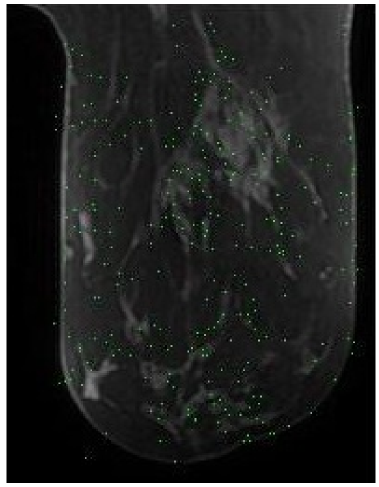

Figure 4.7: Feature points selected by 3DSURF.

the background area. Thus 100 additional control points are uniformly scattered on the background volume to overcome this problem. As a result the total number of control points is 1400. In order to find mesh and image deformation based on the measurements on control points, the exact position of all these points inside mesh must be found. This step must be done prior to the registration, thus its calculation time will not effect the registration time. In our case searching for control points and image grid points (with size of $80 \times 80 \times 80$) took $3s$ and $70s$ respectively. Kalman gain computation time (reduced model with $m = 500$) for 1400 selected control points was $6min$. In Figure 4.8 the displacements at control points in 100^{th} iteration of the registration is shown. The lengths of the blue arrows are proportional to the displacements associated with the corresponding control points. As expected, the deformation is the largest along the horizontal axis, specifically along borders. It can be seen that the background control points are not demonstrating any displacement as expected. Each of the control points and image grid points falls inside one of the mesh elements. The undeformed and deformed mesh is shown in Figure 4.9, and

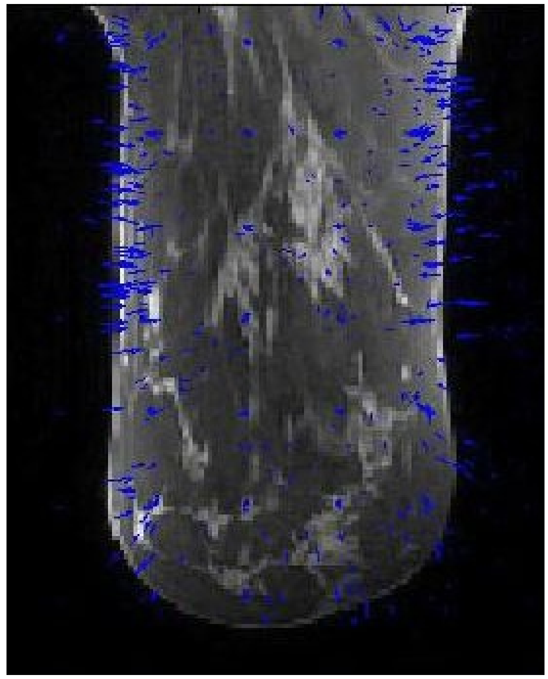

Figure 4.8: Displacement at control points in one iteration of the registration algorithm applied on the template and the reference images(in Figure 4.6)

the reference, template and deformed template images is presented in Figure 4.10. The registration algorithm took $42min$ to complete (reached its maximum number of iteration = 300). .

The results are compared based on the target registration error (TRE) that is obtained based on 12 fiducial points that are manually selected and scattered around the volume of the image. The number of associated control points directly affects the computation cost of the registration method. Using 1440 control points on a regular grid point scattered on the volume of the image has roughly the same computation cost as that of the new method with 1400 selected control points. However, as the data in Table 4.2 illustrates, the registration errors are much larger with a uniform grid of control points. Therefore, it is evident that the efficient distribution of the control

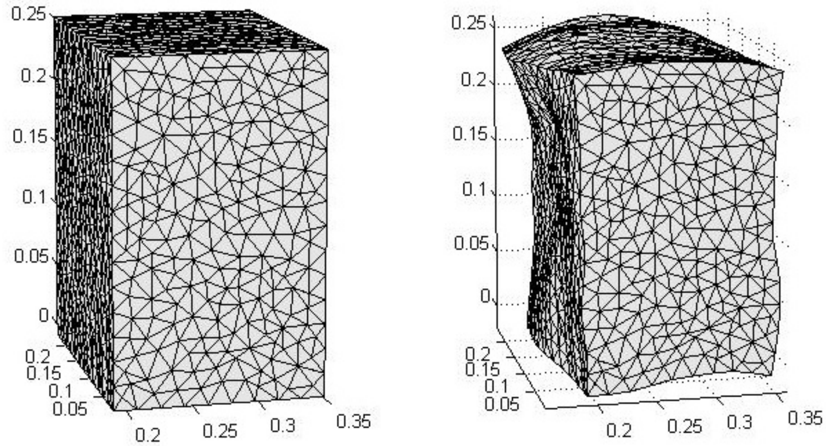

(a) Original Mesh (b) Deformed Mesh

Figure 4.9: The deformed and undeformed mesh using state estimation based image registration algorithm with enhanced control point selection.

points using the new feature selection method improves the registration accuracy.

The data in fourth column of Table 4.2 shows increasing the number of uniform control points to 36000 results in similar performance to that of the new method. However, this is achieved at expense of a significant increase in the computation time. It is noted the registration errors are greater in the x direction , along which the breast is compressed. Registration errors can be further decreased by increasing the number of feature points along the breast image boundaries to produce a more realistic deformation.

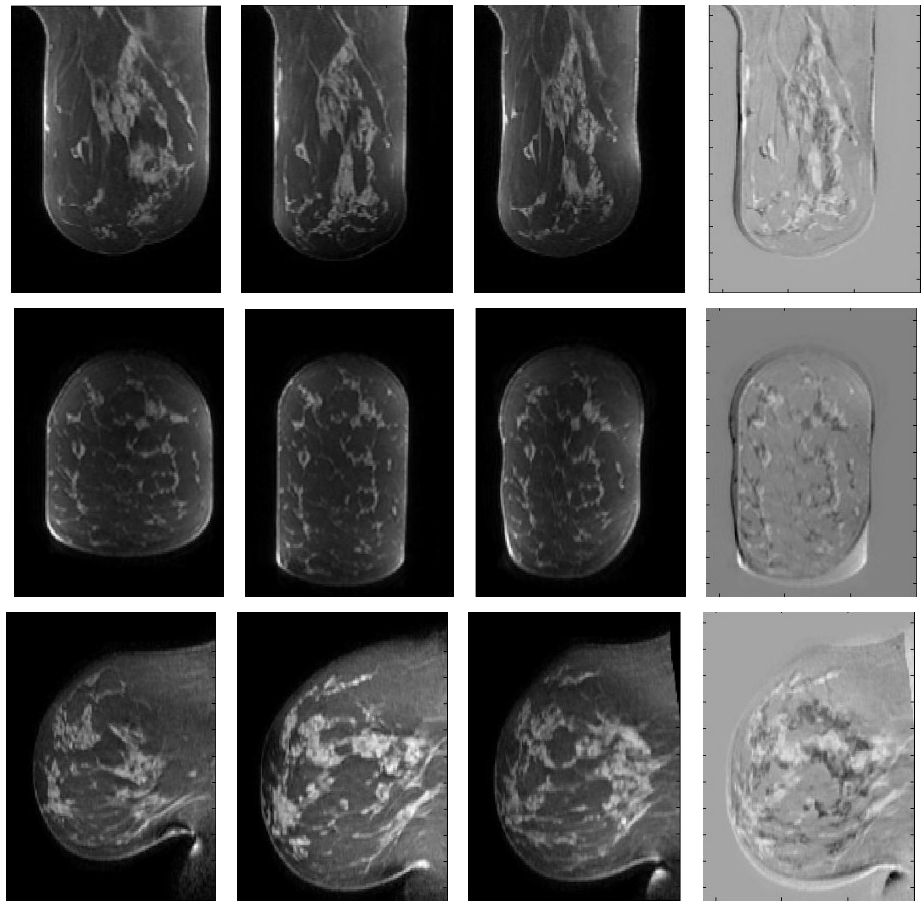

(i) Template (j) Reference (k) Deformed (l) Difference

Figure 4.10: The Template (first row), Reference (second row) and the registered deformed template (third row) in the axial, coronal and sagital view, respectively.

Control Points Selection	Feature Points 1400	Regular Grid $12 \times 12 \times 10$	Regular Grid $30 \times 30 \times 40$	Before
mean $\pm$ std in x	3.22$\pm$1.92	9.31$\pm$ 6.84	2.09$\pm$1.12	11.01$\pm$6.5
mean $\pm$ std in y	1.83$\pm$1.50	2.10$\pm$1.87	1.57$\pm$1.34	2.12$\pm$1.95
mean $\pm$ std in z	3.10$\pm$2.29	7.35$\pm$5.12	2.73$\pm$2.43	8.52$\pm$5.46
mean $\pm$ std	4.13$\pm$2.78	11.43$\pm$4.98	3.61$\pm$2.14	15.89$\pm$5.38

Table 4.2: TRE (in mm) of state estimation based registration method (using CR as similarity measure) with uniform and non-uniform selections of the control points.

Chapter 5

Model-based Deformable Registration

In this chapter, deformable breast image registration is formulated and solved as a nonlinear optimization. A linear static deformation model is used to relate boundary contact forces exerted applied to the breast by the compression plates to the tissue deformation. These unknown contact forces are the optimization decision variables. The objective is to minimize a cost function based on similarity of the reference and deformed template images computed at the image control points. The minimization of this cost function subject to proper constraints on boundary contact forces yields the deformation field that matches the template and reference images. Results of experiments with MRI images of breast demonstrate the effectiveness of the proposed registration algorithm.

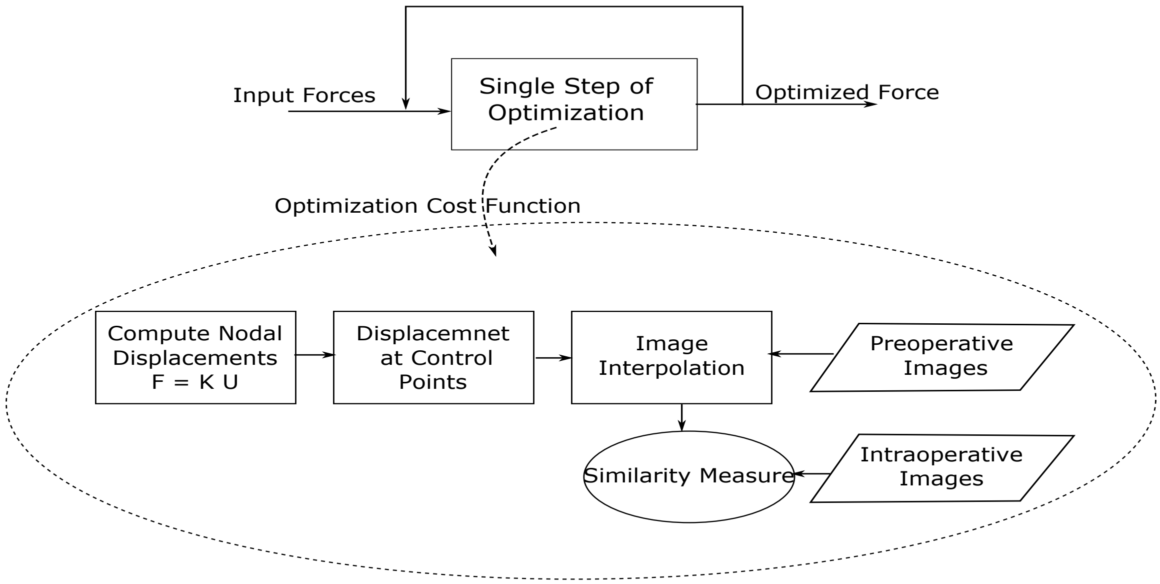

Figure 5.1: Block diagram of the iterative optimization routine

5.1 Overview

In this method, a patient specific finite element model formed over the segmented image volume is used.

An optimization problem is formulated to find boundary contact forces that would minimize a measure of similarity between reference and template images computed at select control points. This is achieved through an iterative search process where the optimization routine produces a candidate vector of contact forces. To this aim a cost function based on the defined similarity measure must be minimized. The flowchart of the iterative optimization loop which is done inside the optimization routine is presented in Figure 5.1 These contact forces are used in the static deformation model in Chapter 3 to deform the 3D finite element mesh and the template image accordingly.

Having the new nodal positions of the FE mesh, the deformed image grid can be obtained using the element shape function The value of the objective function for the given decision variables can be computed by evaluating an image similarity metric between the template and reference images at the control points. The control points are selected using the method proposed in Chapter 4. The optimization routine will continue its search iteratively until an optimal set of contact forces are found to minimize similarity between the deformed template and reference images.

5.2 Registration Method

In the following sections, each of the registration steps are discussed in more details.

5.2.1 Deformation Model

In this thesis, a static deformation model presented in Section 3.2 is employed to relate compression plate contact forces to the deformation of the breast. The goal is to find a set of forces which result in the proper deformation in the template image. Using a biomechanical elastic model discretized in the spatial domain by FEM, by having the applied forces, $\mathbf{f}$, Equation (3.16) needs to be solved in order to find the deformation field, u. In this equation, the stiffness matrix, $\mathbf{K}$, is not full rank when the model is not constrained. Without any boundary conditions, for a 3D FE model with n nodal points, the rank of $\mathbf{K}$ is $3*n-6$. As a result, without setting some constraints on the model, having the forces applied will not necessarily result in a unique displacement field. The constraints can be obtained based on the boundary conditions, e.g., by giving some of the nodes predetermined displacements (Bathe, 2006). In problem considered in this thesis, the nodes near the chest wall are fixed since the breast tissue undergoes very little displacement, if any, around this area. Fixing these nodes in the FE model will require some reformulation of the static equilibrium equations. To illustrate this reformulation, and without loss of generality, a simple case in which the matrix K is 3x3 is considered :

$$\begin{bmatrix} k_{11} & k_{12} & k_{13} \\ k_{21} & k_{22} & k_{23} \\ k_{31} & k_{32} & k_{33} \end{bmatrix} \begin{bmatrix} u_1 \\ u_2 \\ u_3 \end{bmatrix} = \begin{bmatrix} f_1 \\ f_2 \\ f_3 \end{bmatrix}. \tag{5.1}$$

Here first matrix represents the stiffness matrix and **u** and **f** are displacement and force vectors respectively. Now let us assume that the displacement of the second node, u_2 is known. ; therefore the contact force at this node f2 is unknown. The equations can now be re-written in terms of the new vector of unknown variables as follows

$$\begin{bmatrix} k_{11} & 0 & k_{13} \\ k_{21} & -1 & k_{23} \\ k_{31} & 0 & k_{33} \end{bmatrix} \begin{bmatrix} u_1 \\ f_2 \\ u_3 \end{bmatrix} = \begin{bmatrix} f_1 - k_{12}u_2 \\ -k_{22}U \\ f_3 - k_{32}u_2 \end{bmatrix}. \tag{5.2}$$

This simple procedure can be applied to the actual FE mesh of the breast model to impose fixed position boundary constraints at chest wall nodes. Forces at the nodes in proximity of the compression plates are the optimization decision variables, and are unknown. All other nodal forces are set to zero.

5.2.2 Optimization Formulation

The optimization problem for image registration has the following general form

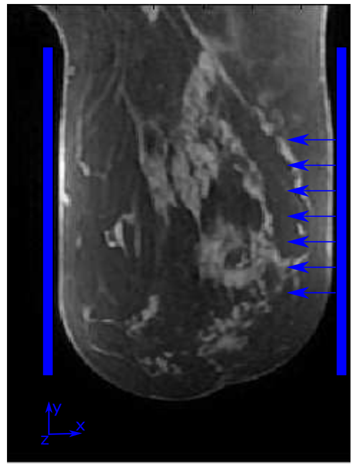

Figure 5.2: Compression plates position.

Our optimization algorithm is formulated as

$$\underset{f}{\text{minimize}} \quad C_0(f) \tag{5.3}$$

where $C_0(f)$ is the cost function to be minimized and f_i is a vector of decision variables. As it is mentioned in the previous section, the contact forces with the compression plates can be chosen as the optimization decision variables. Constraints can be imposed on the amplitude, changes and direction of these forces to ensure they are physically realistic.

As for the force direction, the orientation of the breast and the plates must be considered. The compression plates can be assumed as surfaces parallel to the yz plane which move along the x direction. The relative position of the compression plates to the breast is presented in Figure 5.2. The right plate is the moving one and the left plate is fixed. The moving plate is moved along the blue arrows to compress the breast. This results in forces being applied to both sides of the breast.

Since the compression plates are only in contact with a portion of the breast surface, the nodes of interest must be selected in order to approximate the area of contact properly. The contact area size increases as the breast compressed more. Ideally in the node selection this increase in the area of contact, must be modeled. However, since the optimization cost function and variables are related to the number of involving nodes, inconsistency in this number for each iteration, results in changing the optimization formulation as well and increase the complexity of calculations. Thus a fixed set of nodes needs to be selected. In our modeling we decided to have the selected nodes resembling the final area of contact. For this aim first, an approximated area was selected, after completing the registration algorithm, the nodes that were located at the side in the new deformed mesh are selected as the nodes of interest for running the optimization once again with more precise node selection. While selecting all contact forces, with some extra constraints, seems a logical choice for the decision variables, unfortunately, this could often result in a large optimization problem with significant computations. For instance, an optimization problem with 288 decision variables could result with a typical FE mesh in our problem, if all of the compression plate corresponded nodes were selected. To reduce the number of variables, the contact forces can be approximated by a well-behaved parameterized function.

Fitting node forces to a function has two benefits. First, it speeds up the process of optimization by reducing the number of optimization variables. Second, a proper choice of these parameterizing functions can ensure smoothness of the contact forces without setting any additional constraints. However, reducing the degrees of freedom could negatively impact the accuracy of the registration if the parameterizing function is not selected carefully.

Our numerical experiments show that approximating the contact forces with a mixture of Gaussian functions can yield good registration accuracy. Increasing the number of Gaussian would improve the accuracy, this performance gain is countered by an increase in the computations. A mixture of two Gaussian functions at each side achieves a good balance between accuracy and speed. As a result the forces at each side are represented by

$$f(y,z) = A_1 e^{-\frac{(y-y_{s1})^2}{2\sigma_{y1}^2} - \frac{(z-z_{s1})^2}{2\sigma_{z1}^2}} + A_2 e^{-\frac{(y-y_{s2})^2}{2\sigma_{y2}^2} - \frac{(z-z_{s2})^2}{2\sigma_{z2}^2}} + B, \tag{5.4}$$

where A_1, A_2, B, σ_{y1}, σ_{z1},σ_{y2}, σ_{z2}, y_{s1}, z_{s1} y_{s2} and z_{s2} are unknown and constitute the optimization decision variables. Therefore, the number of optimization variables is reduced to 22 regardless of the number of selected nodes and size of the mesh.

Calculation of Cost Function

In our model the cost function is defined as the similarity measure between the reference image and the deformed template at control points. Control point selection is done by 3D-SURF method similar to the previous chapter. Applying the forces defined in equation (5.4) result in deforming the FE mesh. The displacement field is the solution to the linear system of equations (3.16) after fixing some of its nodes as, discussed in Section 5.2.1. The next step is to find the displacements corresponding to the control points. In this thesis, the control points displacements are calculated by applying Thin Plate Splines (TPS) function introduced in Section 2.3.3. The seed points for TPS are the mesh nodal points, the voxel intensity values of the deformed template at image grid points are the outputs of this function. Lastly, the intensity values of the deformed template are compared to the reference intensities using one of the similarity measures defined in Table 4.1. The value of the similarity measure is the value of the optimization cost function for the given decision variables and provides a basis for the search for the optimal decision variables. In this thesis, the fminsearchbnd from MATLAB, which used Nelder-Mead or downhill simplex, is employed to solve the optimization problem for deformable image registration.

5.2.3 Experiment and Results

Volumetric MR images of normal and compressed healthy breasts are registered together in this section using the proposed registration method. The breast MR images are identical to those of the previous chapter. To develop the finite element model, first the preoperative image of the uncompressed breast is segmented manually using "3D-slicer" software (BWH and contributors, 2014). A combination of global threshold followed by a region growing method and a manual pixel selection (to add/ remove the wrong selected areas), is used for segmentation. Next the segmented image is imported to IA-MESH package of 3D-Slicer to generate a 3D hexahedron mesh model based on the pre-operative uncompressed template breast image. Total number of hexahedron elements and nodes are 881 and 1181, respectively. Youngs elasticity modulus, E, is set to be 3000 Pa, and the Poissons ratio to 0.495 based on data available in the literature (Marami, 2013; Samani *et al.*, 2001). Feature points are selected using 3D-SURF method as done in Chapter 4. Since the FE mesh is formed over the segmented image, in contrast to the previous chapter, there is no need to add the background points in the control point set and 1300 SURF feature points are set as our control points. Setting the boundary conditions requires selecting fixed and side nodes. 144 nodes at each side of the breast are chosen for application of the compression forces in the x direction. The positions of 81 nodes are fixed, representing the chest wall. Selected nodes are shown in Figure 5.3 with black marks. Using equation 5.4 for defining the force distribution yields 11 decision

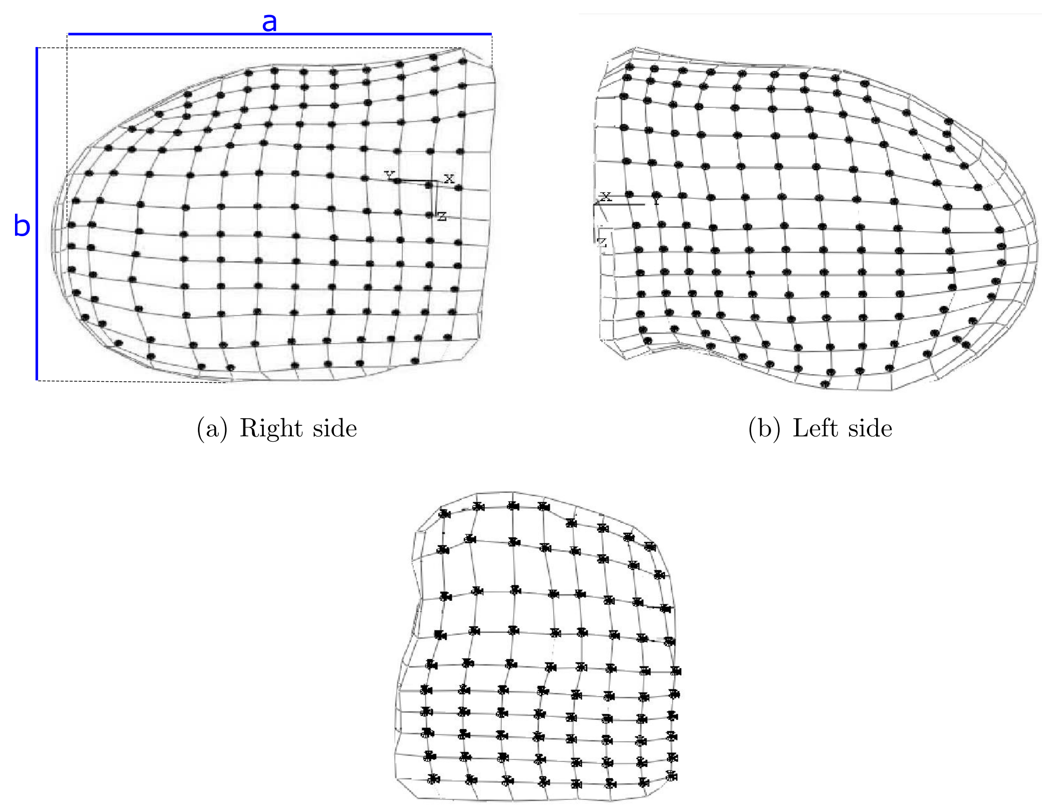

(a) Right side

(b) Left side

(c) Fixed nodes

Figure 5.3: Boundary conditions for the FE mesh:, (a)144 compression force nodes on the right side, (b)144 compression force nodes on the left side (c)88 chest wall nodes with fixed position

variables at each side. However, some of these parameters can be fixed in order to further speed up the optimization process. Applying test forces on different breast side areas and studying the produced deformation fields has shown that the maximum required force needs to be applied near the end of the breast (far side from the chest wall). Our numerical experiments have shown that positioning one of the Gaussians is fixed at [a/4,b/4] from the end of the breast, where a and b are the length of the breast side plates (see Figure 5.3). The other Gaussian is fixed at the center of the compression plate in order to evenly distribute the force to all of the breast area. In addition, the parameter B in Equation 5.4 is also fixed since changes in A_1 and A_2 can produce somewhat similar effect to changes in the parameter B. After fixing these parameters, the number of decision variables are reduced to 12 in total at both sides. These remaining variables are A_1, A_2, σ_{y1},σ_{z1},σ_{y2}, and σ_{z2} in the Equation (5.4) for each side.

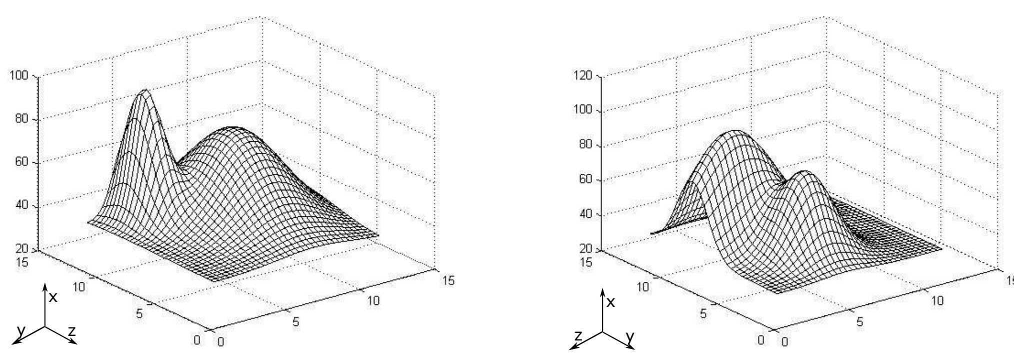

(a) Right Side.

(b) Left Side.

Figure 5.4: Force distribution on the compression plates.

Using SSD for the similarity measure, the optimization algorithm with 12 decision variables takes about one hour to find a solution. This duration for CR is 2.5 and for MI is around 3 hours. These results are based on MATLAB implementation on a 3.4 GHz Intel(R) Core(TM) i7-3770 processor with 32.0 GB RAM.The optimized contact

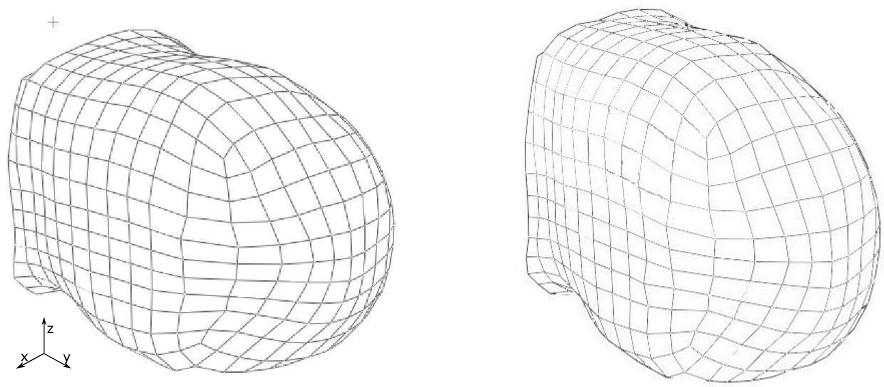

Figure 5.5: Undeformed (left side) and deformed (right side) mesh.

force (for CR method) of the compression plates are shown in Fig. 5.4. The resulting deformation is depicted in Fig. 5.5. The most time consuming part in this model is interpolating the images in order to find the similarity measure. In the TPS method used for interpolation, deformed mesh nodes and some fixed background points are set as seed points. Down-sampling the nodal points in order to decrease the number of seed points can increase the speed of interpolation. However, a reasonable number of seed points are required in order to have the deformation accurately. The extracted optimal force is applied on the finite element mesh. The undeformed and deformed mesh are presented in figure 5.5. Three image views, sagital, axial and coronal of the reference, template and deformed template after registration using CR as similarity measure is presented in Figure 5.6.

Lastly the performance of three similarity measures, SSD, CR, and MI are compared based on target registration error (TRE). The selected fiducial points are the same as previously used in Chapter 4. The results are summarized in Table 5.1 where mean and the standard deviation of these errors are compared. The computed results

Registration Method	SSD	CR	MI	Before
mean ± std in x	1.95±1.23	1.87±1.45	2.01±1.15	11.01±6.5
mean ± std in y	1.41±1.30	1.54±1.21	1.46±1.33	2.12±1.95
mean ± std in z	2.60±2.47	2.52±2.51	2.63±2.39	8.52±5.46
mean ± std	3.58±2.91	3.55±2.96	3.60±2.21	15.89±5.38

Table 5.1: TRE (in mm) of model-based deformable registration method using 3 different similarity measures

are close for all three methods but the best result is associated with CR. The significant difference appears in the computation time. The fastest method is SSD with a factor of almost 2.5 and 3 in compare to CR and M respectively

In this particular example since the resolution of two sets of images(template and reference images) is the same, the performance of SSD is quite similar to CR and MI. However, in clinical application where the intra-operative images are within lower resolution, the SSD performance would decrease compared to two other methods. Hence, there will be a trade off between the speed and accuracy in choosing the type of the similarity measure. Similarly to the results presented in Table 4.2, the maximum measured error stands for the x (compression plates') direction, but the average calculated error using the same similarity metric (CR) is less than the previously introduced method in chapter 4. This can be due to the fact of using model based finite element model and setting boundary condition since the most improvement in the registration results is in the boundary of the image. In addition, using segmented image there is no need to add background control points that affects the error of interpolation method. On the other hand previous algorithm was a noticeably faster method. In the previous chapter using CR as the similarity measure the whole algorithm took half an hour while using the same similarity measure operates 5 times slower with this new method.

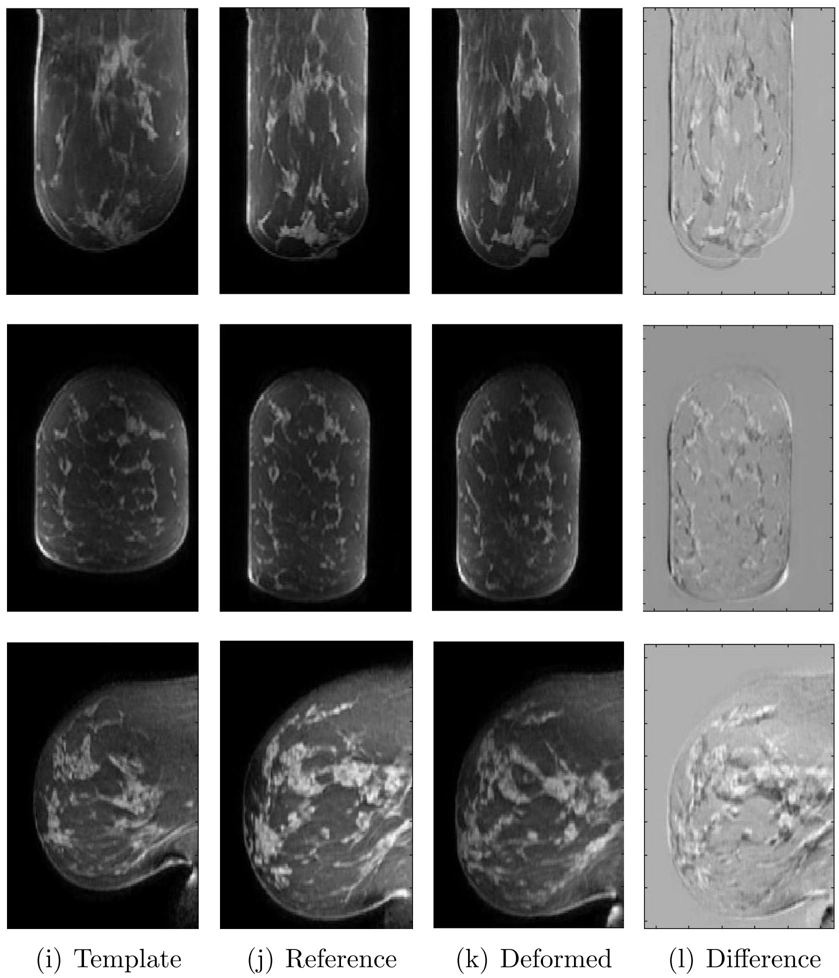

Figure 5.6: The Template (first column), Reference (second column), the registered deformed template (third column), and the difference between the reference image and the final deformed image (forth column) in the axial , coronal and sagital view.

Chapter 6

Conclusions and Future Works

Breast as a soft tissue is subject to significant deformation during compression in diagnostic and interventional MRI breast imaging. Deformable image registration is a vital task for combining information acquired from different images and update the pre-operative information based on the intra-operative image. This thesis was concerned with deformable registration of MRI breast images. New methods were proposed for feature points selection and optimization-based image registration using linear elastic deformation models of the breast tissue.

The first contribution of the thesis was a new method for enhanced selection of the so-called control points in an existing state estimation-based image registration algorithm, previously developed in our group. This registration method uses a FE cubic mesh formed over the whole volume of the image, with tetrahedral elements. The deformation field of the FE mesh is treated as the state vector of a dynamic system, using a dynamic linear elastic deformation model. Estimates of these states are updated through an iterative process using the deformation model and residual prediction errors, approximated by the gradient of a similarity measure between the template and reference images.The similarity measure is computed at the so-called image control points, whose selection can significantly impact the speed and performance of the registration algorithm. Rather than using a uniformly distributed grid of control points, a new method based on a 3D-extension of the popular feature selection method SURF was proposed for choosing the control points.

The next contribution of the thesis was a new model-based deformable image registration method that formulates and solves the problem as an optimization model. A linear elastic FE-based deformation model was constructed based a segmentation of the undeformed template image. Contact forces at the compression plates were parameterized in terms of a number of optimization decision variables. The cost function in the optimization was a similarity measure (i.e., SSD, CR, and MI) between the deformed and template and reference images. The resulting nonlinear optimization was solved by fminsearch algorithm in Matlab to obtain and optimal values for contact forces that would minimize the similarity measure.

These two approaches were successfully applied on the normal and compressed MR images of a healthy woman. The experiment results in Chapter 4 showed that using 3D-SURF selected features for control point selection instead of using regular grid points over the image, decreases the computation time dramatically without sacrificing the performance. The most improvements was in the speed of parameter preparation parts prior to the registration, i.e., Kalman gain calculation and searching algorithm for finding the location of control points inside each finite element. The mean target registration error using CR as the similarity measure for the state estimation based registration method with 1400 3D-SURF selected and regular grid control points was 4.13 and 11.43 mm respectively. This results shows the noticeable influence of selecting control points from the features of the image. However, the performance of registration with 1400, 3D-SURF selected control points was less than having 36000 regular grid control points, specifically in the borders of the breast in the x direction which undergoes maximum deformation. Utilizing same number of 3D-SURF selected control points in the other algorithm presented in Chapter 5, resulted in the mean target registration error of 3.55 mm(for CR similarity measure), where the maximum improvements acquired within the borders. The registration time however, increased from half an hour in Chapter 4 to around 3 hours for the new method.

There are a number of avenues for future research in deformable breast image registration. These include:

- Other image features can be used to improve the control point selection in image registration. One obvious choice would be to extract and include voxels on the boundary of tissue in the control points.
- The evaluation of the methods in this thesis was based on one pair of breast images. An extensive evaluation using a lager set of image data should be carried out to properly validate the results.
- Real-time registration of MRI breast images can be considered during a biopsy procedure where high-rate/small volume/low resolution images are registered to a high-resolution large volume pre-operative image.

- Although the proposed methods have been developed single modality registration, but with some modifications they can be extended to multimodal registration.
- Implementation of the proposed model-based registration method on GPU will benefit the computations from parallel computing and can decrease the registration time to few seconds.

Bibliography

Adler, D. D., Carson, P. L., Rubin, J. M., and Quinn-Reid, D. (1990). Doppler ultrasound color flow imaging in the study of breast cancer: preliminary findings. *Ultrasound in medicine & biology*, **16**(6), 553–559.

Al-Azzawi, N. A., Sakim, H. A. M., and Abdullah, W. A. K. W. (2010). Mr image monomodal registration based on the nonsubsampled contourlet transform and mutual information. In *Computer Applications and Industrial Electronics (ICCAIE), 2010 International Conference on*, pages 481–485. IEEE.

Andronache, A., von Siebenthal, M., Székely, G., and Cattin, P. (2008). Non-rigid registration of multi-modal images using both mutual information and cross-correlation. *Medical image analysis*, **12**(1), 3–15.

Azar, F. S., Metaxas, D. N., and Schnall, M. D. (2001). A deformable finite element model of the breast for predicting mechanical deformations under external perturbations. *Academic Radiology*, **8**(10), 965–975.

Bathe, K.-J. (2006). *Finite element procedures*. Klaus-Jurgen Bathe.

Bay, H., Tuytelaars, T., and Van Gool, L. (2006). Surf: Speeded up robust features. In *Computer Vision–ECCV 2006*, pages 404–417. Springer.

Bookstein, F. L. (1989). Principal warps: Thin-plate splines and the decomposition of deformations. *IEEE Transactions on Pattern Analysis & Machine Intelligence*, (6), 567–585.

Bradley, W. G. (2008). History of medical imaging. *Proceedings of the American Philosophical Society*, pages 349–361.

Broit, C. (1981). Optimal registration of deformed images.

BWH and contributors, D. S. (2014). 3d-slicer. `http://http://www.slicer.or/`. [Online; accessed 19-may-2015].

Chandler, A. G., Pinder, R. J., Netsch, T., Schnabel, J. A., Hawkes, D. J., Hill, D. L., and Razavi, R. (2006). Correction of misaligned slices in multi-slice mr cardiac examinations by using slice-to-volume registration. In *Biomedical Imaging: Nano to Macro, 2006. 3rd IEEE International Symposium on*, pages 474–477. IEEE.

Ellis, R., Caramella, D., and Fadda, M. M. (1996). A biocompatible fiducial marker for evaluating the accuracy of ct image registration. In *Investigative Radiology*. Citeseer.

Felippa, C. A. (2008). Advanced finite element methods. *URL: http://www. colorado. edu/engineering/cas/courses. d/AFEM. d.*

Felippa, C. A. (2013). Advanced finite elements for solids, plates and shells. `http://www.colorado.edu/engineering/CAS/courses.d/AFEM.d/`. [Online; accessed 20-may-2014].

Galloway Jr, R. L., Maciunas, R. J., Edwards, C., *et al.* (1992). Interactive image-guided neurosurgery. *Biomedical Engineering, IEEE Transactions on*, **39**(12), 1226–1231.

Gao, Z., Gu, B., and Lin, J. (2008). Monomodal image registration using mutual information based methods. *Image and Vision Computing*, **26**(2), 164–173.

Gøtzsche, P. C. and Nielsen, M. (2009). Screening for breast cancer with mammography. *Cochrane Database Syst Rev*, **4**(1).

Harris, C. and Stephens, M. (1988). A combined corner and edge detector. In *Alvey vision conference*, volume 15, page 50. Manchester, UK.

Heywang-Köbrunner, S., Viehweg, P., Heinig, A., and Küchler, C. (1997). Contrast-enhanced mri of the breast: accuracy, value, controversies, solutions. *European journal of radiology*, **24**(2), 94–108.

Hill, D. L., Batchelor, P. G., Holden, M., and Hawkes, D. J. (2001). Medical image registration. *Physics in medicine and biology*, **46**(3), R1.

Holden, M., Hill, D. L., Denton, E. R., Jarosz, J. M., Cox, T. C., Rohlfing, T., Goodey, J., and Hawkes, D. J. (2000). Voxel similarity measures for 3-d serial mr brain image registration. *Medical Imaging, IEEE Transactions on*, **19**(2), 94–102.

Hou, M.-F., Chuang, H.-Y., Ou-Yang, F., Wang, C.-Y., Huang, C.-L., Fan, H.-M., Chuang, C.-H., Wang, J.-Y., Hsieh, J.-S., Liu, G.-C., *et al.* (2002). Comparison of breast mammography, sonography and physical examination for screening women at high risk of breast cancer in taiwan. *Ultrasound in medicine & biology*, **28**(4), 415–420.

Inc, C. (2013). Developing fem with comsol. `http://http://www.comsol.com/`. [Online; accessed 8-January-2014].

Jenkinson, M. and Smith, S. (2001). A global optimisation method for robust affine registration of brain images. *Medical image analysis*, **5**(2), 143–156.

Ke, Y. and Sukthankar, R. (2004). Pca-sift: A more distinctive representation for local image descriptors. In *Computer Vision and Pattern Recognition, 2004. CVPR 2004. Proceedings of the 2004 IEEE Computer Society Conference on*, volume 2, pages II–506. IEEE.

Kim, J., Fessler, J., *et al.* (2004). Intensity-based image registration using robust correlation coefficients. *Medical Imaging, IEEE Transactions on*, **23**(11), 1430–1444.

Klein, S., Staring, M., and Pluim, J. P. (2007). Evaluation of optimization methods for nonrigid medical image registration using mutual information and b-splines. *Image Processing, IEEE Transactions on*, **16**(12), 2879–2890.

Kuhl, C. K., Schrading, S., Leutner, C. C., Morakkabati-Spitz, N., Wardelmann, E., Fimmers, R., Kuhn, W., and Schild, H. H. (2005). Mammography, breast ultrasound, and magnetic resonance imaging for surveillance of women at high familial risk for breast cancer. *Journal of clinical oncology*, **23**(33), 8469–8476.

Lee, C. H., Dershaw, D. D., Kopans, D., Evans, P., Monsees, B., Monticciolo, D., Brenner, R. J., Bassett, L., Berg, W., Feig, S., *et al.* (2010). Breast cancer screening with imaging: recommendations from the society of breast imaging and the acr on the use of mammography, breast mri, breast ultrasound, and other technologies for the detection of clinically occult breast cancer. *Journal of the American college of radiology*, **7**(1), 18–27.

Lester, H. and Arridge, S. R. (1999). A survey of hierarchical non-linear medical image registration. *Pattern recognition*, **32**(1), 129–149.

Li, J., Yang, X., and Yu, J. (2007). Compact support thin plate spline algorithm. *Journal of Electronics (China)*, **24**(4), 515–522.

Lowe, D. G. (1999). Object recognition from local scale-invariant features. In *Computer vision, 1999. The proceedings of the seventh IEEE international conference on*, volume 2, pages 1150–1157. Ieee.

Lowe, D. G. (2004). Distinctive image features from scale-invariant keypoints. *International journal of computer vision*, **60**(2), 91–110.

Maes, F., Collignon, A., Vandermeulen, D., Marchal, G., and Suetens, P. (1997). Multimodality image registration by maximization of mutual information. *Medical Imaging, IEEE Transactions on*, **16**(2), 187–198.

Maes, F., Vandermeulen, D., and Suetens, P. (1999). Comparative evaluation of multiresolution optimization strategies for multimodality image registration by maximization of mutual information. *Medical image analysis*, **3**(4), 373–386.

Mafi, R. (2008). Hardware-based parallel computing for real-time simulation of soft-object deformation.

Maintz, J. and Viergever, M. A. (1998). A survey of medical image registration. *Medical image analysis*, **2**(1), 1–36.

Mann, R. M., Kuhl, C. K., Kinkel, K., and Boetes, C. (2008). Breast mri: guidelines from the european society of breast imaging. *European radiology*, **18**(7), 1307–1318.

Marami, B. (2013). Elastic registration of medical images using generic dynamic deformation models.

Modersitzki, J. (2003). *Numerical methods for image registration*. Oxford university press.

Morel, J.-M. and Yu, G. (2009). Asift: A new framework for fully affine invariant image comparison. *SIAM Journal on Imaging Sciences*, **2**(2), 438–469.

Pitiot, A., Bardinet, E., Thompson, P. M., and Malandain, G. (2006). Piecewise affine registration of biological images for volume reconstruction. *Medical image analysis*, **10**(3), 465–483.

Pluim, J. P. (2000). Mutual information based registration of medical images. *Ponsen & Looijen*, pages p22–p25.

Roche, A., Malandain, G., Pennec, X., and Ayache, N. (1998a). The correlation ratio as a new similarity measure for multimodal image registration. In *Medical Image Computing and Computer-Assisted InterventationMICCAI98*, pages 1115–1124. Springer.

Roche, A., Malandain, G., Ayache, N., Pennec, X., *et al.* (1998b). Multimodal image registration by maximization of the correlation ratio.

Roche, A., Pennec, X., Rudolph, M., Auer, D., Malandain, G., Ourselin, S., Auer, L. M., and Ayache, N. (2000). Generalized correlation ratio for rigid registration of 3d ultrasound with mr images. In *Medical Image Computing and Computer-Assisted Intervention–MICCAI 2000*, pages 567–577. Springer.

Rueckert, D., Sonoda, L. I., Hayes, C., Hill, D. L., Leach, M. O., and Hawkes, D. J. (1999). Nonrigid registration using free-form deformations: application to breast mr images. *Medical Imaging, IEEE Transactions on*, **18**(8), 712–721.

Samani, A., Bishop, J., Yaffe, M. J., and Plewes, D. B. (2001). Biomechanical 3-d finite element modeling of the human breast using mri data. *Medical Imaging, IEEE Transactions on*, **20**(4), 271–279.

Samavati, N. (2009). Deformable multi-modality image registration based on finite element modeling and moving least squares.

Santamaría, J., Cordón, O., and Damas, S. (2011). A comparative study of state-of-the-art evolutionary image registration methods for 3d modeling. *Computer Vision and Image Understanding*, **115**(9), 1340–1354.

Sarrut, D. and Miguet, S. (1999). Similarity measures for image registration. In *In First European Workshop on Content-Based Multimedia Indexing*. Citeseer.

Saslow, D., Boetes, C., Burke, W., Harms, S., Leach, M. O., Lehman, C. D., Morris, E., Pisano, E., Schnall, M., Sener, S., *et al.* (2007). American cancer society guidelines for breast screening with mri as an adjunct to mammography. *CA: a cancer journal for clinicians*, **57**(2), 75–89.

Schnall, M. D. (2003). Breast mr imaging. *Radiologic Clinics of North America*, **41**(1), 43–50.

Schneider, R. J., Perrin, D. P., Vasilyev, N. V., Marx, G. R., del Nido, P. J., and Howe, R. D. (2012). Real-time image-based rigid registration of three-dimensional ultrasound. *Medical image analysis*, **16**(2), 402–414.

Shen, D. and Davatzikos, C. (2002). Hammer: hierarchical attribute matching mechanism for elastic registration. *Medical Imaging, IEEE Transactions on*, **21**(11), 1421–1439.

Simon, D., Otoole, R., Blackwell, M., Morgan, F., DiGioia, A., and Kanade, T. (1995). Accuracy validation in image-guided orthopaedic surgery. In *Second Annual Intl. Symp. on Med. Rob. an Comp-Assisted surgery, MRCAS*, volume 95, pages 185–192. Citeseer.

Solberg, O. V., Lindseth, F., Torp, H., Blake, R. E., and Hernes, T. A. N. (2007). Freehand 3d ultrasound reconstruction algorithmsa review. *Ultrasound in medicine & biology*, **33**(7), 991–1009.

Solomentsev, E. (2011). Interpolation process.

Sotiras, A., Davatzikos, C., and Paragios, N. (2013). Deformable medical image registration: A survey. *Medical Imaging, IEEE Transactions on*, **32**(7), 1153–1190.

Studholme, C., Hill, D. L., and Hawkes, D. J. (1999). An overlap invariant entropy measure of 3d medical image alignment. *Pattern recognition*, **32**(1), 71–86.

Suetens, P. (2009). *Fundamentals of medical imaging*. Cambridge university press.

Viola, P. and Wells III, W. M. (1997). Alignment by maximization of mutual information. *International journal of computer vision*, **24**(2), 137–154.

Woods, R. P., Grafton, S. T., Watson, J. D., Sicotte, N. L., and Mazziotta, J. C. (1998). Automated image registration: Ii. intersubject validation of linear and nonlinear models. *Journal of computer assisted tomography*, **22**(1), 153–165.

Zagorchev, L. and Goshtasby, A. (2006). A comparative study of transformation functions for nonrigid image registration. *Image Processing, IEEE Transactions on*, **15**(3), 529–538.

Zienkiewicz, O. C. and Taylor, R. L. (2000). *The finite element method: Solid mechanics*, volume 2. Butterworth-heinemann.

Zienkiewicz, O. C., Taylor, R. L., Zienkiewicz, O. C., and Taylor, R. L. (1977). *The finite element method*, volume 3. McGraw-hill London.